

17 Active Nordic Seas deep-water formation during the last  
18 glacial maximum

19 Christina S. Larkin<sup>1,2,3\*</sup>, Mohamed M. Ezat<sup>1,4,5</sup>, Natalie L. Roberts<sup>1</sup>, Henning A.  
20 Bauch<sup>6,7</sup>, Robert F. Spielhagen<sup>7</sup>, Riko Noormets<sup>8</sup>, Leonid Polyak<sup>9</sup>, Steven G.  
21 Moreton<sup>10</sup>, Tine L. Rasmussen<sup>4</sup>, Michael Sarnthein<sup>11</sup>, Edward T. Tipper<sup>1</sup>, Alex M.  
22 Piotrowski<sup>1,3</sup>

23 Affiliations:

24 <sup>1</sup>Department of Earth Sciences, University of Cambridge, Downing Street, UK.

25 <sup>2</sup>School of Ocean and Earth Science, University of Southampton, National

26 Oceanography Centre, UK. <sup>3</sup>Murray Edwards College, University of Cambridge,

27 Huntingdon Road, Cambridge, UK. <sup>4</sup>CAGE – Centre for Arctic Gas Hydrate,

28 Environment and Climate, Department of Geosciences, UiT the Arctic University of

29 Norway, Tromsø, Norway. <sup>5</sup>Department of Geology, Faculty of Science, Beni-Suef

30 University, Beni-Suef, Egypt. <sup>6</sup>Alfred Wegener Institute for Polar and Marine

31 Research, Bremerhaven, Germany. <sup>7</sup>GEOMAR Helmholtz Centre for Ocean

32 Research, Kiel, Germany. <sup>8</sup>The University Centre in Svalbard, Norway. <sup>9</sup>Byrd Polar

33 and Climate Research Center, Ohio State University, USA <sup>10</sup>NERC Radiocarbon

34 Facility, East Kilbride, UK. <sup>11</sup>Christian-Albrechts University, Kiel, Germany. \*e-mail:

35 c.s.larkin@soton.ac.uk

36 **The Nordic Seas are the primary location where the warm waters of the North**  
37 **Atlantic Current densify to form North Atlantic Deep Water, which plays a key**  
38 **part in the modern Atlantic Meridional Overturning Circulation. The formation**

39 of dense water in the Nordic Seas and Arctic Ocean and resulting ocean  
40 circulation changes were likely driven by and contributed to the regional and  
41 global climate of the last glacial maximum (LGM). Here, we map the source and  
42 degree of mixing of deep-water in the Nordic Seas, and through the Arctic  
43 Gateway (Yermak Plateau) over the last 35 thousand years using neodymium  
44 isotopes ( $\epsilon\text{Nd}$ ) measured on authigenic phases in deep-sea sediments with a  
45 high spatial and temporal resolution. We find that a large-scale reorganisation  
46 of deep-water formation in the Nordic Seas took place between the LGM (23-18  
47 thousand years ago) and the rapid climate shift that accompanied the  
48 subsequent deglaciation (18-10 thousand years ago). We show that  
49 homogeneous  $\epsilon\text{Nd}$  signatures across a wide range of sites support LGM deep-  
50 water formation in the Nordic Seas. In contrast, during the deglaciation  
51 disparate and spatially variable  $\epsilon\text{Nd}$  values are observed leading to the  
52 conclusion that deep-water formation may have been reduced during this time.

53

54 Deep-water formation processes in the Nordic Seas regulate the global climate via  
55 the redistribution of heat by the surface ocean and the capacity of the deep ocean to  
56 store carbon<sup>1</sup>. At present the Atlantic Meridional Overturning Circulation (AMOC)  
57 links polar and sub-polar climate with the formation of North Atlantic Deep Water  
58 (NADW), a major component of the global oceanic thermohaline circulation. The  
59 densest northern-sourced waters in the modern AMOC are formed in the Nordic  
60 Seas, primarily by deep convection and gradual transformation of North Atlantic  
61 surface waters<sup>2</sup>.

62

63 These dense waters formed in the modern Nordic Seas overflow the Greenland-  
64 Scotland Ridge (GSR), eventually contributing to NADW accumulating carbon and  
65 nutrients as it flows throughout the deep ocean<sup>2</sup> (Fig. 1). The extent, mechanism,  
66 and importance of deep-water formation in the Nordic Seas during glacial periods  
67 and periods of ice rafting during meltwater events (Heinrich Events/Heinrich Stadials)  
68 are still not adequately understood. The canonical view is that the glacial AMOC was  
69 displaced from the Nordic Seas to south of Iceland in the form of a fast and shallow  
70 overturning cell forming Glacial North Atlantic Intermediate Water and that there was  
71 Southern-sourced water in the deep (> 2.5 km) Atlantic<sup>e.g.3</sup>. Contrary to this several  
72 studies<sup>e.g.4,5</sup> argue for the presence of glacial NADW and speculate that this dense  
73 water may have been sourced from the Nordic Seas. Keigwin and Swift<sup>6</sup> similarly  
74 suggest that a Northern-sourced water mass may have been present in the deep (~  
75 5000 m) Atlantic, which could plausibly have been sourced from the Nordic Seas<sup>7</sup>.  
76 However, proposed scenarios of LGM deep-water formation in the Nordic Seas  
77 range from near-cessation to vigorous present-day-like deep-water formation<sup>8-11</sup>.

78

79 There is evidence supporting a continued or intermittent subsurface inflow of the  
80 North Atlantic Current (NAC) during the LGM<sup>12,13</sup> to the Norwegian Sea. Polynya  
81 formation proximal to ice-sheets has been inferred, ventilating parts of the LGM deep  
82 Nordic Seas<sup>7,9,14</sup>. Several proxy studies indicate a persistent overflow from the  
83 Nordic Seas into the glacial Atlantic Ocean<sup>8,15,16</sup>. However, warmer waters (~ 1 to  
84 2°C warmer than the modern) in the intermediate to deep Nordic Seas and  
85 Arctic<sup>11,17,18</sup> indicate a reduced heat release to the atmosphere and less net cooling  
86 of the NAC waters, which could be due to subsurface expansion and deepening of  
87 the NAC<sup>13,19</sup>. This does not support widespread deep-water formation by brine

88 rejection or modern-like open-ocean convection, which would produce cooler waters  
89 at depth. Nevertheless, periodic cooler bottom water temperatures have been  
90 observed in LGM-aged sediments near Svalbard and in the Lofoten Basin<sup>18,20</sup>. Less  
91 efficient deep-water formation via convective processes, upwelling, slow modification  
92 and return of Atlantic waters, or small-scale brine formation at shelf edges could be  
93 consistent with studies to date.

94

95 Ultimately, the question of Nordic Seas deep-water formation during the LGM and its  
96 geographical extent remains an open debate which has not yet been fully  
97 constrained by proxy studies. Resolving the location and extent of deep-water  
98 formation under glacial conditions is key to understanding the link between climate,  
99 the oceans, ice-sheets, heat transport and carbon cycling. In this study, therefore,  
100 we provide, at a high spatial and temporal resolution, a depiction of past Nordic Seas  
101 circulation under glacial conditions.

102

### 103 **Neodymium isotope tracing of ocean circulation**

104 Neodymium (Nd) isotopes measured on authigenic phases (authigenic  $\epsilon\text{Nd}$ ) are a  
105 powerful tool used to trace water mass circulation<sup>21</sup>.  $\epsilon\text{Nd}$  is a proxy of the source of  
106 the Nd in the water mass. Spatial records can be related to each other to trace the  
107 flow path of water masses, and deduce their mixing with other water masses, so long  
108 as new sources of Nd are not added. However, the local input of Nd to water  
109 masses<sup>22,23</sup> can also alter the dissolved seawater  $\epsilon\text{Nd}$  composition. This is likely to  
110 be of greater relative importance in controlling spatial patterns of  $\epsilon\text{Nd}$  during times of  
111 reduced advection.



112 We measured  $\epsilon\text{Nd}$  on mixed planktic foraminifera, which were not reductively  
113 cleaned of authigenic coatings and thus represent bottom water<sup>24</sup>, and weak acid-  
114 reductive sediment leaches from a wide range of deep-sea sediment core sites in the  
115 Arctic Ocean and Nordic Seas. This is combined with published records to produce a  
116 high spatial and temporal resolution (Fig. 1) allowing us to place the magnitude of  
117 proxy shifts into a regional context and distinguish large scale changes linked to  
118 hydrographic transport and mixing from small-scale variability due to local inputs.  
119 Detailed information on samples and analytical methods is given in the Methods and  
120 Extended Data Figures 1,2,3 and 4.

121 Previous proxy studies in this region have often focused on only a handful of core  
122 sites. Traditional proxy studies (e.g.  $\delta^{13}\text{C}$ ) based on epifaunal benthic foraminifera  
123 are hampered by the scarcity of suitable foraminifera in this region and, therefore,  
124 lack a holistic approach. Moreover, studies based on palaeotemperature  
125 reconstructions and radiocarbon ventilation ages fail to provide information on larger-  
126 scale, long-term, water-mass homogenisation and extent and, therefore, direct  
127 evidence for prolonged deep-water formation and its geographical range. Sea  
128 surface temperature and biomarker studies and studies based on foraminiferal  
129 calcite have the potential to be biased by highly variable year-on-year and seasonal  
130 conditions<sup>25</sup>, potentially masking a true, time-integrated climate and oceanographic  
131 signature. Our approach, in contrast, provides a different insight because it  
132 integrates seasonal and multi-annual variability.  $\epsilon\text{Nd}$  integrates longer-term ocean  
133 processes due to the relatively long residence time of Nd in the ocean ( $\sim 200\text{-}1000$   
134 years) and the way the signature is continually incorporated into sediments in early  
135 authigenic phases, making it sensitive to hydrographic changes which occur on this  
136 timescale.

137

138 **High resolution  $\epsilon$ Nd**

139

140 We measured authigenic  $\epsilon$ Nd in 17 core sites to map out the geographical extent  
141 and consistency, or inconsistency, of Nordic Sea water-mass compositions from the  
142 last glacial period ( $\sim 35$  ka) to the late Holocene ( $< 5$  ka). Individual core records  
143 from selected high-resolution core sites are shown in Fig. 2. Data are compared to  
144 similar records from the NE Atlantic and central Arctic Ocean as records in Fig. 2  
145 and are also presented as time-slice cross sections in Fig. 3. Due to the high  
146 resolution of this data set and to understand the larger scale pattern of  $\epsilon$ Nd, the data  
147 are temporally averaged. The data group naturally into 3 equal sized (5 ka) time  
148 intervals (Fig. 4), comprising the late Holocene (5-0 ka), the deglaciation (18-13 ka)  
149 and the LGM (23-18 ka). This compilation is focused on the Nordic Seas and Arctic  
150 Gateway (Yermak Plateau). The data are shown as probability density plots and  
151 histograms (Fig. 4). We compare the late Holocene with seawater values from the  
152 same depth and latitudinal range (Fig. 4), as well as to the LGM and deglacial  
153 values. These datasets were also compared using statistical tests (details are given  
154 in the Methods and Extended Data Fig. 5 and Extended Data Tables 1 and 2).

155

156 The late Holocene compositions (0-5 ka) observed in the Nordic Seas and Yermak  
157 Plateau show the same spatial patterns (Fig 3A,B) and variability (Fig 4) as the  
158 modern across a range of core sites from the shallowest (at 488 m water depth,  
159 today bathed in warm northward flowing Atlantic waters on the Yermak Plateau) to  
160 the deepest in the Greenland Sea (3050 m water depth). This demonstrates that for  
161 the late Holocene, a seawater-derived signature is recorded with  $\epsilon$ Nd on authigenic

162 phases. In addition, the similar spatial pattern to the modern implies a hydrographic  
163 link between the inflow and deeper regions in the Nordic Seas and the Yermak  
164 Plateau. The homogeneity of the modern and late Holocene dataset relative to the  
165 large Nd isotope range of potential sources (which span almost the entire crustal  
166 array of  $\epsilon\text{Nd}$ ,  $\sim -40$  on Greenland, to  $\sim 10$  on Iceland) also indicates vigorous  
167 circulation acting to homogenize compositions in the Nordic Sea, with a value of  $\sim$ -  
168 10 (Fig. 4).

169

170 The Yermak Plateau provides the ideal locality to test for changes in the NAC  
171 composition over time, because this is where warm high salinity Atlantic-derived sub-  
172 surface waters are in contact with the sediment-water interface<sup>26,27</sup>. A shallow  
173 sediment core from the Yermak Plateau (Fig. 2c, at 488 m) is used to monitor past  
174 changes in this Atlantic-derived endmember. Many studies indicate the continued  
175 strong influence of warm Atlantic waters in this region at the LGM, including at this  
176 core site<sup>12,26</sup>. We compare this shallow core site to two other cores at different water  
177 depths (798 m and 2531 m). These Yermak Plateau cores sites have differing  
178 sedimentation rates (4, 6 and 10 cm/kyr) and likely distinctive sediment  
179 provenances<sup>28</sup>. All the sites show similar changes through time (Fig. 2c). The three  
180 core sites are hydrographically linked in the modern ocean by vigorous circulation  
181 and the influence of Atlantic-derived waters across the Arctic Ocean<sup>27</sup>. The Holocene  
182  $\epsilon\text{Nd}$  at these three core sites are within error of modern compositions<sup>29,30</sup>.

183

184 During the LGM the Yermak Plateau  $\epsilon\text{Nd}$  averages to  $-13.1 \pm 0.9$  ( $2\sigma$  (standard  
185 deviation) with a similar homogeneity and stability to the late Holocene but  
186 systematically offset in composition. The strong co-variation between these sites and

187 the homogeneous LGM and Holocene compositions (Fig. 2C) indicates that these  
188 sites are recording an advected seawater signature resulting from Atlantic inflow and  
189 deep-water mixing and not localised sediment inputs or pore fluid processes. While  
190 some mixing with fresh and intermediate waters and localized inputs of Nd from  
191 sediment may change the NAC  $\epsilon\text{Nd}$  along its pathway, the homogeneity of the  
192 signature at the LGM supports deep-water mixing that dominates over any local  
193 process. The LGM  $\epsilon\text{Nd}$  at the Yermak Plateau is within error of modern composition  
194 of the NAC as it enters the Nordic Seas ( $-12.9 \pm 1.1$  ( $2\sigma$  (standard deviation)<sup>31</sup>),  
195 suggesting that this signature might be derived entirely from Atlantic waters.  
196 However, the past NAC endmember composition is unknown, and it may well have  
197 changed. The similar standard deviation of LGM  $\epsilon\text{Nd}$  (Fig 2c) as the modern,  
198 regardless of the absolute value, over several residence times of Nd in the ocean,  
199 implies that at least the shallow site records the LGM NAC composition entering the  
200 Arctic Ocean, and that the deeper sites reflect deep-water mixing of this signature. In  
201 addition to previous evidence for the influence of Atlantic waters at the Yermak  
202 Plateau during the LGM<sup>12</sup>, these core sites indicate that authigenic  $\epsilon\text{Nd}$  records an  
203 active NAC inflow as well as transfer of these waters to depth at the Yermak Plateau  
204 during the LGM.

205

#### 206 **Last glacial maximum homogeneity**

207

208 The LGM Yermak Plateau  $\epsilon\text{Nd}$  is similar to the rest of the Nordic Seas data (Fig. 1,  
209 4). LGM compositions from this region approximate to a normal distribution (Fig. 4,  
210 Methods) with a standard deviation similar to the late Holocene and modern  
211 seawater, suggesting that there was a common water source at these sites at

212 different time periods. Therefore, the core sites were hydrographically connected  
213 during the LGM. The link between the NAC at the Yermak Plateau and the deep  
214 Nordic Seas indicates that there was widespread transformation of Atlantic waters to  
215 depth. Our LGM data, therefore, indicates the influence of the Atlantic-derived waters  
216 at the Nordic Seas and Yermak Plateau sites. The temperature over much of the  
217 deep to intermediate Nordic Seas during the LGM was  $\sim 1$  to  $2^{\circ}\text{C}$  warmer than the  
218 modern<sup>11,13</sup>, suggesting a lower net of cooling of high salinity NAC waters and a  
219 reduced heat release to the atmosphere. Although more recent evidence suggests  
220 there were periodically cooler bottom water temperatures during the LGM in the  
221 Nordic Seas (e.g., near Svalbard<sup>18,20</sup>), which may reflect periodic and localized  
222 higher efficiency cooling. We infer that the overall efficiency of surface to deep water  
223 transformation was likely less than it is today, with moderately ventilated overflows  
224 and deep waters<sup>16,32</sup>. Homogeneous Nordic Seas LGM  $\epsilon\text{Nd}$  is interpreted as  
225 evidence for deep-water formation. Our interpretation is that this deep-water  
226 formation was probably a mixture of processes which are likely to have been  
227 temporally variant. It is important to note that these findings represent time-  
228 integrated averages and, therefore, show the continued dominant advective control  
229 on  $\epsilon\text{Nd}$  over thousands of years, despite highly variable sea-surface and sea-ice  
230 conditions<sup>25</sup>. The homogeneity of seawater  $\epsilon\text{Nd}$  compositions in this region show  
231 that they were not locally changed by significant ice-rafted or other local sediment or  
232 benthic inputs during the LGM, as potential source compositions are large<sup>e.g.,22,33</sup>.

233

234 The processes affecting  $\epsilon\text{Nd}$  in this region during the deglacial were different to both  
235 the modern and LGM (Fig. 4). In contrast to the narrow normally distributed  $\epsilon\text{Nd}$   
236 during the modern and LGM there is a wide (standard deviation = 4.4, Fig. 4) non-

237 normal (Methods, Extended Data Fig. 5 and Table 1) distribution during the  
238 deglaciation, suggesting that local Nd inputs with highly variable  $\epsilon\text{Nd}$  dominated the  
239 sources of Nd, outcompeting homogenisation by deep-water mixing. Although there  
240 is consistency in the shift seen between some sites (Yermak Plateau, Central  
241 Norwegian Sea, Fig. 2), other sites show disparate compositions (Fig. 2, Fig. 4). The  
242 reason for this change may be a result of a mixture of two indistinguishable  
243 processes: firstly, an increased sedimentary and freshwater input of Nd with variable  
244 compositions into the basin and, secondly, a decrease or shutdown of deep-water  
245 formation processes, which both lead to a dominance of localised sources of Nd at  
246 several sites.

247

#### 248 **Connectivity to the Atlantic**

249

250 Our data provide evidence for vigorous homogenisation of Nd throughout the water  
251 column leading to the conclusion that LGM deep-water was widespread across the  
252 central and eastern Nordic Seas and Yermak Plateau. Such widespread deep-water  
253 coupled with previous observations of moderately ventilated overflows to the east of  
254 Iceland<sup>16</sup> means that this deep-water was exported to the Atlantic. However, since a  
255 similar signature to the Nordic Seas is not seen in the NE Atlantic (Figs. 2 and 3),  
256 non-conservative processes (changing seawater  $\epsilon\text{Nd}$  via input of Nd sourced from  
257 local sediment) may mask the  $\epsilon\text{Nd}$  record of export to the NE Atlantic<sup>24,34</sup>. This  
258 dense water could also have exited the Nordic Seas via the Denmark Strait, as has  
259 been previously suggested<sup>18,35</sup>; however, no suitable  $\epsilon\text{Nd}$  records have yet been  
260 obtained from the Denmark Strait.

261

262 It is possible that the deep-water formed in the Nordic Seas ventilated parts of the  
263 deep Atlantic, explaining previous observations of northern-sourced bottom water in  
264 the NW Atlantic<sup>6,36,37</sup>. Conceivably the Nordic Seas may have been the source of the  
265 ventilated dense water mass at 5 km depth observed in the NW Atlantic by Keigwin  
266 and Swift<sup>6</sup> and not the Labrador Sea as previously suggested.

267

268 These findings are of importance to the ongoing debate on the structure and nature  
269 of glacial-interglacial changes in Atlantic overturning and its link to climate, as it  
270 suggests that the Nordic Seas remained a critical source of dense water to the  
271 Atlantic during the LGM. Our dataset provides a benchmark for future AMOC  
272 modelling studies that use earth system models with Nd isotopes and infer LGM  
273 changes in the strength of deep-water formation in the Nordic Seas. The evidence  
274 presented herein indicates that LGM deep-water formation in the Nordic Seas was  
275 relatively widespread, and that deep-water mixing was vigorous enough to  
276 outcompete and homogenise other sources of Nd, rather than being confined to  
277 localised small scale processes.

278

## 279 **Acknowledgments**

280 C.S.L. thanks T. Williams, V. Rennie, R. Wang and M-L. Bagard, J. Hall, S.  
281 Crowhurst, G. Dipre and H. Chapman for assistance in the lab. C.S.L. is grateful to  
282 K. Hogan and C. Xuan for suggesting core locations. The British Ocean Sediment  
283 Core Research Facility, the Byrd Polar and Climate Research Center, Lamont-  
284 Doherty Core Repository and International Ocean Discovery Program are thanked  
285 for supplying sediment samples used in this study. C.S.L was funded by a NERC  
286 studentship (NE/L002507/1), with support from Murray Edwards College and the  
287 Geological Society's Elspeth Matthews Fund. Radiocarbon analysis was supported

288 by NERC Radiocarbon Facility NRCF010001 to A.M.P, S.G.M and C.S.L (allocation  
289 number 2117.0418). MME is funded by the Research Council of Norway and the Co-  
290 funding of Regional, National, and International Programmes (COFUND) – Marie  
291 Sklodowska-Curie Actions under the EU Seventh Framework Programme (FP7),  
292 project number 274429, and the Tromsø Research Foundation, project number  
293 A31720. MME and TLR received funding from the Research Council of Norway  
294 through its Centres of Excellence funding scheme, grant number 223259.

295

### 296 **Author Contributions**

297 The research was planned by C.S.L, A.M.P, E.T.T., with input from all authors.  
298 Analysis was carried out by C.S.L, apart from as follows: data from core PS1243 was  
299 obtained by N.L.R. Materials were supplied by H.A.B, R.F.S, L.P, T.L.R, M.S, R.N  
300 and M.M.E. The manuscript was written by C.S.L. with comments and contributions  
301 from all authors.

### 302 **Competing Interests**

303 The authors declare no competing interests.

304 **Correspondence and requests for materials** should be addressed to C.S.L

305 (c.s.larkin@soton.ac.uk).

### 306 **Figure Captions**

307 **Fig. 1. Deep-sea sediment core locations.** a, Map showing core sites: red squares  
308 (records) and circles (core tops) measured in this study, blue diamonds are literature  
309 data<sup>22,24,33,38–40</sup>. Crossed blue circles represent sites of convection. Orange arrows



310 show near surface/intermediate currents: North Atlantic Current (NAC), East  
311 Greenland Current (EGC); blue arrows show deep currents: Arctic Intermediate  
312 Water (AIW), Denmark Strait Overflow Water (DSOW), Iceland-Scotland Overflow  
313 Water (ISOW), Wyville-Thomson Ridge Overflow Water (WTROW), Labrador Sea  
314 Water (LSW), North Atlantic Deep Water (NADW). The approximate extent of ice  
315 sheets (blue dashed line<sup>41</sup>) and the Arctic Ocean at the LGM (black dashed line<sup>42</sup>)  
316 are shown. Grey arrows represent the modern water inputs: major rivers, the  
317 Greenland ice-sheet, and Pacific derived water (PDW)<sup>29</sup>. **b**, Cross section. NAC  
318 flows into the eastern Nordic Seas (orange arrow), where convection occurs (light  
319 blue arrows). Deepwater flow (dark blue arrow) feeds into NADW (grey crossed  
320 circle indicates westward flow). Made using Ocean Data View (ODV)<sup>43</sup>.

321

322 **Fig. 2. Arctic Ocean, Nordic Seas and NE Atlantic neodymium isotope recon-**  
323 **structions over the last 35 ka. a**, Map of core locations: diamonds, literature data;  
324 squares, this study. Colours match symbols for records in B-G. **b**, Arctic Ocean  $\epsilon\text{Nd}$ :  
325 purple circles, Laptev Sea; white circles, Lomonosov Ridge<sup>39</sup>; black circles,  
326 Mendeleev Ridge<sup>40</sup>. **c**, Yermak Plateau  $\epsilon\text{Nd}$ : yellow, dark blue, and light blue. **d**,  
327 Northern Norwegian Sea  $\epsilon\text{Nd}$ <sup>22</sup>. **e**, Central Norwegian Sea:  $\epsilon\text{Nd}$ , dark blue (this  
328 study); light blue<sup>22</sup>. **f**, Eastern Norwegian Sea  $\epsilon\text{Nd}$ : purple and pink, Vøring Plateau;  
329 orange, Lofoten Basin. **g**, Greenland Sea  $\epsilon\text{Nd}$ . **h**, NE Atlantic mixed planktic  
330 foraminifera: grayscale lines<sup>24,38</sup>. **i**, North Greenland ice core  $\delta^{18}\text{O}$ <sup>44</sup>, YD: Younger  
331 Dryas, HS1–3: Heinrich Stadials 1–3, blue bars indicate these intervals. Orange box  
332 is the modern NAC composition entering the Nordic Seas<sup>31</sup>. **b-f**, circles are sediment  
333 leachates, squares are foraminifera. Typical  $2\sigma$  (standard deviation)  $\epsilon\text{Nd}$  errors are  
334 smaller or equal to the symbol size.

335

336 **Fig. 3 Time-slice reconstructions of Arctic Ocean, Nordic Seas and North East**

337 **Atlantic  $\epsilon\text{Nd}$ .** **a**, Modern seawater  $\epsilon\text{Nd}^{29-31,45-50}$ . **b**, Core top/late Holocene

338 authigenic  $\epsilon\text{Nd}$ . **c**, Time-slice authigenic  $\epsilon\text{Nd}$  average during the LGM, 23–18 ka,

339 grey dots in **a-c** are locations of data points (core sites and modern seawater

340 sampling). **d**, Map showing location of cross section (X-Y, black dashed line),

341 maximum extent of data used in  $\epsilon\text{Nd}$  profiles (red line), and locations of data points

342 (blue dots, core sites and modern seawater locations). Figure was created with ODV.

343 White boxes indicate areas with a lack of data. Data used in **b** and **c** is summarised

344 in Supplementary Table S7.

345 **Fig. 4. Histogram and probability distribution of Nordic Seas and Yermak**

346 **Plateau  $\epsilon\text{Nd}$ .** Data is split into 5 ka time intervals: late Holocene (5–0 ka, light red,

347 data from 14 different core sites), deglacial (18–13 ka, orange, data from 10 different

348 core sites), LGM (23–18 ka, blue, data from 12 different core sites). Modern

349 seawater compositions over the same depth and latitudinal range as core sites (i.e.,

350 excluding near-surface seawater data) are also shown<sup>29,31,46</sup> (dark red). Bin-width is

351 1 epsilon unit and dashed lines indicate the means. Mean of the deglacial range is

352 not shown. Authigenic  $\epsilon\text{Nd}$  data includes data from this study, Maccali *et al.*<sup>33</sup> and,

353 Struve *et al.*<sup>22</sup>. Means and associated  $2\sigma$  errors are given.

354

## 355 **References**

356 1. Aagaard K., Swift J. H. & Carmack E. C. Thermohaline circulation in the Arctic  
357 Mediterranean Seas. *J. Geophys. Res. Oceans* **90**, 4833–4846 (1985).

358 2. Hansen, B. & Østerhus, S. North Atlantic–Nordic Seas exchanges. *Prog.*

359 *Oceanogr.* **45**, 109–208 (2000).

- 360 3. Rahmstorf, S. Ocean circulation and climate during the past 120,000 years.  
361 *Nature* **419**, 207–214 (2002).
- 362 4. Howe, J. N. W. *et al.* North Atlantic Deep Water Production during the Last Glacial  
363 Maximum. *Nat. Commun.* **7**, 11765 (2016).
- 364 5. Oppo, D. W. *et al.* Data Constraints on Glacial Atlantic Water Mass Geometry and  
365 Properties. *Paleoceanogr. Paleoclimatology* **33**, 1013–1034 (2018).
- 366 6. Keigwin, L. D. & Swift, S. A. Carbon isotope evidence for a northern source of  
367 deep water in the glacial western North Atlantic. *Proc. Natl. Acad. Sci.* **114**, 2831–  
368 2835 (2017).
- 369 7. Ezat, M. M., Rasmussen, T. L., Skinner, L. C. & Zamelczyk, K. Deep ocean  $^{14}\text{C}$   
370 ventilation age reconstructions from the Arctic Mediterranean reassessed. *Earth*  
371 *Planet. Sci. Lett.* **518**, 67–75 (2019).
- 372 8. Veum, T., Jansen, E., Arnold, M., Beyer, I. & Duplessy, J.-C. Water mass  
373 exchange between the North Atlantic and the Norwegian Sea during the past  
374 28,000 years. *Nature* **356**, 783 (1992).
- 375 9. Bauch, H. A. *et al.* A multiproxy reconstruction of the evolution of deep and  
376 surface waters in the subarctic Nordic seas over the last 30,000yr. *Quat. Sci. Rev.*  
377 **20**, 659–678 (2001).
- 378 10. Hoffmann, S. S., McManus, J. F., Curry, W. B. & Brown-Leger, L. S.  
379 Persistent export of  $^{231}\text{Pa}$  from the deep central Arctic Ocean over the past 35,000  
380 years. *Nature* **497**, 603–606 (2013).
- 381 11. Thornalley, D. J. R. *et al.* A warm and poorly ventilated deep Arctic  
382 Mediterranean during the last glacial period. *Science* **349**, 706–710 (2015).

- 383 12. Nørgaard-Pedersen, N. *et al.* Arctic Ocean during the Last Glacial Maximum:  
384 Atlantic and polar domains of surface water mass distribution and ice cover.  
385 *Paleoceanography* **18**, 1063 (2003).
- 386 13. Ezat, M. M., Rasmussen, T. L. & Groeneveld, J. Persistent intermediate water  
387 warming during cold stadials in the southeastern Nordic seas during the past 65  
388 k.y. *Geology* **42**, 663–666 (2014).
- 389 14. Knies, J. *et al.* Nordic Seas polynyas and their role in preconditioning marine  
390 productivity during the Last Glacial Maximum. *Nat. Commun.* **9**, 1–10 (2018).
- 391 15. Yu, J., Elderfield, H. & Piotrowski, A. M. Seawater carbonate ion- $\delta^{13}\text{C}$   
392 systematics and application to glacial–interglacial North Atlantic ocean circulation.  
393 *Earth Planet. Sci. Lett.* **271**, 209–220 (2008).
- 394 16. Ezat, M. M. *et al.* Ventilation history of Nordic Seas overflows during the last  
395 (de)glacial period revealed by species-specific benthic foraminiferal  $^{14}\text{C}$  dates.  
396 *Paleoceanography* **32**, 172–181 (2017).
- 397 17. Cronin, T. M. *et al.* Deep Arctic Ocean warming during the last glacial cycle.  
398 *Nat. Geosci.* **5**, 631–634 (2012).
- 399 18. Ezat, M. M. *et al.* Deep Ocean Storage of Heat and  $\text{CO}_2$  in the Fram Strait,  
400 Arctic Ocean During the Last Glacial Period. *Paleoceanogr. Paleoclimatology* **36**,  
401 e2021PA004216 (2021).
- 402 19. Rasmussen, T. L. & Thomsen, E. Warm Atlantic surface water inflow to the  
403 Nordic seas 34–10 calibrated ka B.P. *Paleoceanography* **23**, (2008).
- 404 20. Altuna, N. E. bani, Ezat, M. M., Greaves, M. & Rasmussen, T. L. Millennial-  
405 Scale Changes in Bottom Water Temperature and Water Mass Exchange  
406 Through the Fram Strait  $79^\circ\text{N}$ , 63–13 ka. *Paleoceanogr. Paleoclimatology* **36**,  
407 e2020PA004061 (2021).

- 408 21. Frank, M. Radiogenic isotopes: Tracers of past ocean circulation and  
409 erosional input. *Rev. Geophys.* **40**, (2002).
- 410 22. Struve, T. *et al.* Ice-sheet driven weathering input and water mass mixing in  
411 the Nordic Seas during the last 25,000 years. *Earth Planet. Sci. Lett.* **514**, 108–  
412 118 (2019).
- 413 23. Abbott, A. N. A benthic flux from calcareous sediments results in non-  
414 conservative neodymium behavior during lateral transport: A study from the  
415 Tasman Sea. *Geology* **47**, 363–366 (2019).
- 416 24. Roberts, N. L. & Piotrowski, A. M. Radiogenic Nd isotope labeling of the  
417 northern NE Atlantic during MIS 2. *Earth Planet. Sci. Lett.* **423**, 125–133 (2015).
- 418 25. Müller, J. & Stein, R. High-resolution record of late glacial and deglacial sea  
419 ice changes in Fram Strait corroborates ice–ocean interactions during abrupt  
420 climate shifts. *Earth Planet. Sci. Lett.* **403**, 446–455 (2014).
- 421 26. Chauhan, T., Rasmussen, T. L. & Noormets, R. Palaeoceanography of the  
422 Barents Sea continental margin, north of Nordaustlandet, Svalbard, during the last  
423 74 ka. *Boreas* **45**, 76–99 (2016).
- 424 27. Rudels, B. *et al.* The interaction between waters from the Arctic Ocean and  
425 the Nordic Seas north of Fram Strait and along the East Greenland Current:  
426 results from the Arctic Ocean-02 Oden expedition. *J. Mar. Syst.* **55**, 1–30 (2005).
- 427 28. Chauhan, T., Noormets, R. & Rasmussen, T. L. Glaciomarine sedimentation  
428 and bottom current activity on the north-western and northern continental margins  
429 of Svalbard during the late Quaternary. *Geo-Mar. Lett.* **36**, 81–99 (2016).
- 430 29. Laukert, G. *et al.* Ocean circulation and freshwater pathways in the Arctic  
431 Mediterranean based on a combined Nd isotope, REE and oxygen isotope section  
432 across Fram Strait. *Geochim. Cosmochim. Acta* **202**, 285–309 (2017).

- 433 30. Andersson, P. S. *et al.* Neodymium isotopes in seawater from the Barents  
434 Sea and Fram Strait Arctic–Atlantic gateways. *Geochim. Cosmochim. Acta* **72**,  
435 2854–2867 (2008).
- 436 31. Lacan, F. & Jeandel, C. Neodymium isotopic composition and rare earth  
437 element concentrations in the deep and intermediate Nordic Seas: Constraints on  
438 the Iceland Scotland Overflow Water signature. *Geochem. Geophys. Geosystems*  
439 **5**, Q11006 (2004).
- 440 32. Telesiński, M. M., Ezat, M. M., Muschitiello, F., Bauch, H. A. & Spielhagen, R.  
441 F. Ventilation History of the Nordic Seas Deduced From Pelagic-Benthic  
442 Radiocarbon Age Offsets. *Geochem. Geophys. Geosystems* **22**, e2020GC009132  
443 (2021).
- 444 33. Maccali, J., Hillaire-Marcel, C., Carignan, J. & Reisberg, L. C. Geochemical  
445 signatures of sediments documenting Arctic sea-ice and water mass export  
446 through Fram Strait since the Last Glacial Maximum. *Quat. Sci. Rev.* **64**, 136–151  
447 (2013).
- 448 34. Vogt-Vincent, N., Lippold, J., Kaboth-Bahr, S. & Blaser, P. Ice-rafted debris as  
449 a source of non-conservative behaviour for the  $\epsilon\text{Nd}$  palaeotracer: insights from a  
450 simple model. *Geo-Mar. Lett.* (2020) doi:10.1007/s00367-020-00643-x.
- 451 35. Millo, C., Sarnthein, M., Voelker, A. & Erlenkeuser, H. Variability of the  
452 Denmark Strait Overflow during the Last Glacial Maximum. *Boreas* **35**, 50–60  
453 (2006).
- 454 36. Pöppelmeier, F. *et al.* Influence of Ocean Circulation and Benthic Exchange  
455 on Deep Northwest Atlantic Nd Isotope Records During the Past 30,000 Years.  
456 *Geochem. Geophys. Geosystems* **20**, 4457–4469 (2019).

- 457 37. Blaser, P. *et al.* Labrador Sea bottom water provenance and REE exchange  
458 during the past 35,000 years. *Earth Planet. Sci. Lett.* **542**, 116299 (2020).
- 459 38. Crocker, A. J. *et al.* Geochemical response of the mid-depth Northeast  
460 Atlantic Ocean to freshwater input during Heinrich events 1 to 4. *Quat. Sci. Rev.*  
461 **151**, 236–254 (2016).
- 462 39. Haley, B. A., Frank, M., Spielhagen, R. F. & Eisenhauer, A. Influence of brine  
463 formation on Arctic Ocean circulation over the past 15 million years. *Nat. Geosci.*  
464 **1**, 68–72 (2008).
- 465 40. Jang, K. *et al.* Glacial freshwater discharge events recorded by authigenic  
466 neodymium isotopes in sediments from the Mendeleev Ridge, western Arctic  
467 Ocean. *Earth Planet. Sci. Lett.* **369–370**, 148–157 (2013).
- 468 41. Spielhagen, R. Glaciology: Enigmatic Arctic ice sheets. *Nature* **410**, 427–428  
469 (2001).
- 470 42. Clark, P. U. *et al.* The Last Glacial Maximum. *Science* **325**, 710–714 (2009).
- 471 43. Schlitzer, R. Ocean Data View, [odv.awi.de](http://odv.awi.de), (2021).  
472
- 473 44. NGRIP Project Members. High-resolution record of Northern Hemisphere  
474 climate extending into the last interglacial period. *Nature* **431**, 147 (2004).
- 475 45. Dubois-Dauphin, Q. *et al.* Fingerprinting Northeast Atlantic water masses  
476 using neodymium isotopes. *Geochim. Cosmochim. Acta* **210**, 267–288 (2017).
- 477 46. Lacan, F. & Jeandel, C. Subpolar Mode Water formation traced by  
478 neodymium isotopic composition. *Geophys. Res. Lett.* **31**, (2004).
- 479 47. Laukert, G. *et al.* Transport and transformation of riverine neodymium isotope  
480 and rare earth element signatures in high latitude estuaries: A case study from the  
481 Laptev Sea. *Earth Planet. Sci. Lett.* **477**, 205–217 (2017).

- 482 48. Werner, K., Frank, M., Teschner, C., Müller, J. & Spielhagen, R. F. Neoglacial  
483 change in deep water exchange and increase of sea-ice transport through eastern  
484 Fram Strait: evidence from radiogenic isotopes. *Quat. Sci. Rev.* **92**, 190–207  
485 (2014).
- 486 49. Zimmermann, B. *et al.* Hafnium isotopes in Arctic Ocean water. *Geochim.*  
487 *Cosmochim. Acta* **73**, 3218–3233 (2009).
- 488 50. Porcelli, D. *et al.* The distribution of neodymium isotopes in Arctic Ocean  
489 basins. *Geochim. Cosmochim. Acta* **73**, 2645–2659 (2009).

490

#### 491 **Methods**

492 Deep-sea sediment cores used in this study were obtained as listed in the  
493 Supplementary Table S1.

494

495 **Authigenic neodymium isotopes.** Authigenic Nd isotopes were measured on either  
496 sediment leachates and/or mixed species of planktic foraminifera. Mixed planktic  
497 foraminifera were not reductively cleaned but had clay particles removed following<sup>24</sup>  
498 and references therein. In short, mixed planktic foraminifera were picked from the  
499 coarse fraction (> 63 µm) and then crushed between two glass plates, rinsed,  
500 sonicated and any clays removed. The samples were then dissolved in 1M glacial  
501 acetic acid.

502

503 Marine sediment was leached with a weak acid-reductive leach in order to extract  
504 the seawater-derived hydrogenic ferromanganese (oxy)hydroxide phases following  
505 the significantly improved method of Blaser *et al.*<sup>51</sup>. In brief, a 5mM hydroxylamine  
506 hydrochloride-3mM Na-EDTA-1.5% acetic acid leach buffered to a pH of ~4 with



507 NaOH was reacted with dry sediment. The following modifications from Blaser *et*  
508 *al.*<sup>51</sup> were made: 1–2 g of sediment was leached in 10 mls of reagent instead of 0.3–  
509 0.4 g, and the reaction time was reduced to 20–30 minutes. These modifications  
510 improved the sample/reagent ratio and reduced even further the likelihood of  
511 leaching into the detrital fraction<sup>52</sup>. Unless otherwise stated, sediment leaches were  
512 carried out on bulk sediment. A small number of sediment leaches were carried out  
513 on the fine fraction (<63 µm) in addition to the bulk, as noted in Supplementary Table  
514 S4. There was no significant difference between bulk sediment leachates and fine  
515 fraction leachates carried out at the same depth, as both agree within uncertainty.  
516 Nd was extracted using established ion-exchange chromatographic procedures: rare  
517 earth elements were extracted using TRUspec resin, and Nd was then separated  
518 from the other rare earth elements using Eichrom LNspec resin<sup>4</sup>. Neodymium  
519 isotopes were measured on a Thermo Fischer Neptune Plus MC-ICP-MS at the  
520 University of Cambridge Department of Earth Sciences, apart from mixed planktic  
521 foraminifera from core PS1243, which were measured on a Nu Plasma HR-MC-ICP-  
522 MS. <sup>146</sup>Nd/<sup>144</sup>Nd was normalised to 0.7219, and samples were run with a  
523 concentration-matched solution of reference standard JNdi-1 and were corrected to  
524 the accepted value of JNdi-1: <sup>143</sup>Nd/<sup>144</sup>Nd=0.512115<sup>53</sup>. The εNd of each sample is  
525 quoted alongside the external error (2σ) (Supplementary Tables S4), which is 2  
526 times the standard deviation on replicate measurements of the concentration  
527 matched JNdi-1 reference standard across the corresponding measurement session  
528 (typically 6–12 hours long). εNd was calculated in parts per 10,000 relative to the  
529 chondritic uniform reservoir, <sup>143</sup>Nd/<sup>144</sup>Nd<sub>CHUR</sub>=0.512638<sup>54</sup>. Longer-term external  
530 and internal reproducibility was monitored using digested US Geological Survey  
531 (USGS) rock standards, with a least one standard analysed per analytical session

532 and standards being regularly passed through column chemistry at the same time as  
533 samples. Rock standards measured were as follows: BHVO-2  $\epsilon\text{Nd}=6.78\pm0.17$  ( $2\sigma$ ),  
534  $n=14$ , BCR-2  $\epsilon\text{Nd}=-0.1\pm0.26$  ( $2\sigma$ ),  $n=14$ , SCO-1  $\epsilon\text{Nd}=-10.48\pm0.27$  ( $2\sigma$ ),  $n=8$ . All 3  
535 rock standards are within error of previously published values: BHVO-2  
536  $\epsilon\text{Nd}=6.75\pm0.21$  ( $2\sigma$ ), BCR-2  $\epsilon\text{Nd}=-0.02\pm0.23$  ( $2\sigma$ )<sup>55</sup>, SCO-1  $\epsilon\text{Nd}=-10.77\pm0.57$   
537 ( $2\sigma$ )<sup>56</sup>. Full procedural replicates reproduced values within uncertainty.  
538 3 full procedural (2 leachates, and one foraminifera) and 2 column chemistry blanks  
539 were determined by isotope dilution using either a  $^{150}\text{Nd}$  or  $^{146}\text{Nd}$  spike measured on  
540 either a TIMS VG Sector 54 in ion counting mode or a Neptune Plus MC-ICP-MS.  
541 Samples were not blank corrected as blanks ranged from 6–26 pg, representing  
542  $\leq 0.5\%$  of all sample sizes analysed.

543

544 **Reliability of bulk sediment leachates.** The reliability of bulk sediment leachates  
545 as tracers of past seawater  $\epsilon\text{Nd}$  was tested by comparing core top values to those of  
546 modern seawater compositions and foraminifera measured at the same core depth.  
547 Core top values are closely correlated with the closest published seawater value.  
548 Seawater values alongside core top measurements are summarised in Extended  
549 Data Fig. 1. Foraminiferal  $\epsilon\text{Nd}$  and bulk sediment leachates from the same depth are  
550 compared in Extended Data Fig. 1. Both foraminiferal and bulk sediment leachates  
551 values are in close agreement over a wide range of  $\epsilon\text{Nd}$ .

552

553 Concentrations of a suite of major and some trace elements were monitored in  
554 several of the sediment leachates (across a wide range of  $\epsilon\text{Nd}$  compositions) in  
555 order to check for detrital contamination following Blaser *et al.*<sup>51</sup>. Leachate samples  
556 were measured using a matrix-matched calibration line made of single elemental

557 standards on an Agilent Technologies ICP-OES in the Department of Earth  
558 Sciences, University of Cambridge. External reproducibility was monitored using  
559 certified standards SPS-SW2 (Spectrapure Standards AS, Oslo, Norway) and a  
560 digested USGS rock standard BCR-2, diluted with a matrix matched blank leach  
561 solution; values obtained with their deviation from certified values are summarised in  
562 Supplementary Table S2. Nd concentrations  $< \sim 2$  ppb were below detection, and  
563 samples were analysed at  $> 4$  ppb Nd. A mixture of single element standards was  
564 used to monitor instrumental drift. The ratios of Al/Nd and Sr/Ca were calculated and  
565 compared to the normal 'hydrogenic' range as defined by<sup>51,57</sup> (Sr/Ca (mg/g)  $> 2$ ,  
566 Al/Nd (g/g)  $\sim < 110$ ), none of the leachates analysed fell significantly outside this  
567 range suggesting no significant detrital contamination (Supplementary Table S3).

568

569 **Age Models.** Existing published age models used in this study are summarised in  
570 Supplementary Table 5.

571

572 Core GIK23074 is tied to the Lake Suigetsu record using  $^{14}\text{C}$  plateau tuning<sup>58</sup> and is  
573 put on the U-Th model age timescale of Bronk Ramsey *et al.*<sup>59</sup> in calendar years  
574 before present (BP). Age models from the Nordic Seas and Arctic Ocean reliant on  
575 radiocarbon dating were recalculated using the Marine13 calibration, since the  
576 Marine20 data set is not considered suitable for samples from polar regions<sup>60</sup>, with  
577 Bayesian Age-Depth Modelling software 'BACON' v.2.3.3 in R<sup>61</sup> (Extended Data Fig.  
578 2, supplementary Table S5) with appropriate surface reservoir age corrections  
579 (supplementary Table S5). The maximum and minimum ages shown in  
580 supplementary data tables are the 95% confidence intervals. The age used is the  
581 mean age and is given in calendar years before present. Several cores with more

582 poorly constrained age models<sup>62–64</sup> were selected for time slice (LGM and Holocene)  
583 measurements only, as outlined in supplementary Table S1.

584

585 Radiocarbon ages were obtained for HLY0503-22-TC and PS2212-3 on mixed  
586 planktic foraminifera (*N. pachyderma*, *T. quinqueloba*) picked from the > 63 µm  
587 fraction. Preparation of samples was carried out with the assistance of technical staff  
588 at the NERC Radiocarbon Facility. The outer 20% (by weight) of shell was removed  
589 by controlled hydrolysis with dilute HCl. The samples were then rinsed in deionised  
590 water, dried, and homogenised. A known weight of the sample was hydrolysed to  
591 CO<sub>2</sub> using 85% orthophosphoric acid at room temperature. The CO<sub>2</sub> was converted  
592 to graphite by Fe/Zn reduction. δ<sup>13</sup>C was measured on a dual inlet stable isotope  
593 mass spectrometer (Thermo Fisher Delta V). Radiocarbon ages were obtained by  
594 technical staff at the Scottish Universities Environmental Research Centre  
595 accelerator mass spectrometer (AMS). One low mass sample (0.337 mg carbon)  
596 was obtained by technical staff at the Keck Carbon Cycle AMS Facility, University of  
597 California, Irvine. Radiocarbon ages obtained are summarised in Supplementary  
598 Table S6. These uncalibrated radiocarbon ages were input into ‘BACON’ Bayesian  
599 Age-Depth Modelling software in R<sup>61</sup> where they were calibrated automatically using  
600 the Marine13 calibration. An appropriate surface ocean reservoir age correction was  
601 also input for each date<sup>58,65</sup> and is summarised in Supplementary Table S6.

602 Additional tie points were also included: HLY0503-22-TC was tied to the previously  
603 dated piston core deployed at the same time (HLY0503-22-JPC<sup>66</sup>) using magnetic  
604 susceptibility, and PS2212-3 was tied to nearby dated cores using a synchronous  
605 mineralogical event—Event I—characterised by the presence of ordered-layered  
606 expandable minerals (OLEM)<sup>67</sup>. The synthesised age scale produced using

607 'BACON', which takes into consideration the error in the radiocarbon calibration, is  
608 shown alongside new  $\epsilon\text{Nd}$  data in the supplementary data tables. The age taken is  
609 the mean, and the 95% confidence interval is shown as the maximum and minimum  
610 age.

611

612 Core PS1243 has been tied to records from the southern Norwegian Sea, which  
613 have been tied to the North Greenland Ice Core Project (NGRIP), based upon  
614 planktic  $\delta^{18}\text{O}$ <sup>11</sup>. The  $\epsilon\text{Nd}$  data from Struve *et al.*<sup>22</sup> has been put on the slightly  
615 modified age scale of core PS1243 from Ezat *et al.*<sup>16</sup>, in which PS1243 was aligned  
616 to core JM11-FI-19PC using planktic  $\delta^{18}\text{O}$ . The independent chronology of JM11-FI-  
617 19PC is based on several proxy alignments to Greenland ice cores in addition to  
618 tephra layers that are common to Greenland ice cores. PS1243 has been placed on  
619 the Greenland Ice Core Chronology 2005 time scale (GICC05<sup>68</sup>), and ages have  
620 been converted from b2k to years BP.

621

622 The age model originally used for core JM06-WP-16-MC<sup>33</sup> in the western Fram Strait  
623 relied on radiocarbon ages, and the authors did not make any assumption about  
624 surface reservoir age when constructing the age model. Surface reservoir ages in  
625 this region are likely to have been variable and potentially very large, particularly  
626 during the deglaciation<sup>11,58</sup>. In order to make this record comparable with the  
627 timescales used in this study, the radiocarbon ages are recalibrated with reasonable  
628 surface reservoir age corrections from Thornalley *et al.*<sup>11</sup>, and the age depth model  
629 is reconstructed using 'BACON' in the same way as for new and recalculated age-  
630 depth scales for new data presented in this study. This recalculation shifts data  
631 points which were originally considered to be LGM in age to substantially younger

632 ages. These data points are now deglacial (< 18 ka) in age, and the record is,  
633 therefore, directly comparable with other records in this study. The rest of the age  
634 models used for literature data are the same as in the original papers<sup>22,24,38</sup>.  
635  
636 These differing methods for obtaining age models are comparable over the time  
637 scales of interest (on the order of several hundreds to thousands of years) because  
638 of the similarity in the planktic  $\delta^{18}\text{O}$  records<sup>9,13,69–72</sup> (Extended Data Fig. 3). However,  
639 differing resolutions in and types of age models mean that not all records may  
640 necessarily be directly comparable on centennial timescales. There is likely to be  
641 unknown uncertainty that is not necessarily covered by the bayesian age-depth  
642 modelling approach. Above all, marine reservoir ages are likely to have been  
643 significant and variable over the timescale of interest, and although some  
644 assumptions are made based on several previous studies to ensure comparability,  
645 these assumptions have unknown and large errors. For this reason, the whole  
646 dataset is considered primarily as averages over 1000's of years, rather than  
647 comparing smaller scale temporal shifts. Despite these shortcomings, the dataset  
648 resolution is sufficient to enable comparisons over the timescales of interest.

649

650 **Synthesis and statistical analysis.** Deep-sea sediment core sites were chosen for  
651 higher resolution records based upon the presence of existing well-defined age  
652 models and/or high sedimentation rates. A series of core sites were analysed only  
653 for their core top compositions (Fig.1, supplementary table S1) to compare with  
654 modern seawater compositions. Several cores with lower-resolution age models  
655 were analysed only at the LGM and Holocene. New  $\epsilon\text{Nd}$  measurements were  
656 obtained primarily from weak acid-reductive sediment leaches, with additional

657 measurements on non-chemically cleaned mixed planktic foraminifera where  
658 possible, from this wide range of sediment core sites in the Arctic Ocean and Nordic  
659 Seas (supplementary table S1). The new  $\epsilon\text{Nd}$  records are combined with three  
660 published records from the Nordic Seas for analysis (Fig. 4). To understand the  
661 larger scale patterns of  $\epsilon\text{Nd}$  in this region, all data (including literature data) north of  
662 the GSR in the Nordic Seas and at the Yermak Plateau (sites as shown in Extended  
663 Data Fig. 4) are split into 3 equal time intervals, comprising the late Holocene (5-0  
664 ka), the deglaciation (18-13 ka) and the LGM (23-18 ka). There is insufficient data  
665 from too few core sites to adequately characterise the data in this manner > 23 ka.  
666 The data is averaged and shown as probability density estimates and histograms  
667 (Fig. 4). The late Holocene is compared with seawater values from the same depth  
668 and latitudinal range as well as to the LGM and deglacial values. The late Holocene  
669 data is within error of the modern seawater array. The LGM values average to a  
670 composition which is systematically offset from the Late Holocene by between -2.7  
671 and -2.2 epsilon units (95% confidence intervals), but with a similar spread ( $2\sigma = 1.2$   
672 and 1.1 respectively). Although the deglacial average is within error of the Late  
673 Holocene, values are disparate, and the spread is large ( $2\sigma = 4.4$ ).

674 Simple statistical tests were applied to the averaged datasets shown in Fig. 4 to  
675 compare their distributions both in terms of absolute compositions and structure.  
676 Means, variances, and distributions (normal/non-normal) were compared and  
677 appropriate statistical tests carried out in R.

678

679 Kernel density estimates (probability distributions) shown in Fig. 4 show that the late  
680 Holocene, seawater, and LGM datasets approximate to normal distributions. The  
681 deglacial dataset, in comparison, forms a flattened distribution with a greater

682 standard deviation to the LGM, modern, and Holocene data. This deviation from the  
683 normal distribution seen at the LGM and Holocene is not caused by sampling  
684 limitations as the sample size is large (n=96).

685

686 The Shapiro-Wilk test of normality was applied to each of the  $\epsilon\text{Nd}$  datasets  
687 (Extended Data Table 1). If this test is significant (p-value < 0.05), the distribution is  
688 non-normal. The late Holocene, seawater, and LGM arrays are all shown to be not  
689 significantly different from a normal distribution. The deglacial data is confirmed to be  
690 non-normally distributed. Quantile-quantile normal plots additionally indicated  
691 normality (no significant departures from the 1:1 line as all points lie within the 95%  
692 error envelope) for the late Holocene, seawater, and LGM datasets and indicated  
693 significant departures from the 1:1 line for the deglacial dataset (Extended Data Fig.  
694 5).

695

696 The variances of the distributions shown to be normal (modern seawater, late  
697 Holocene, and LGM) with similar standard deviations (Fig. 4) are compared using an  
698 F-test (Extended Data Table 2). This assesses whether the scatter (spread) in each  
699 of these datasets is comparable. The F-test assesses the ratio of the variances of  
700 two datasets. The closer to  $F=1$  the more likely the data have equal population  
701 variances. If the test is significant (p-value < 0.05), the two distributions have  
702 differing variances. The LGM and Late Holocene datasets have similar variances.  
703 This, combined with the Shapiro-Wilk test, implies similarity in both the width and the  
704 type of distribution of these datasets, despite differing means (Fig. 4).

705



706 The late Holocene and modern seawater datasets have significantly different  
707 variances, and the seawater dataset has a lower standard deviation when compared  
708 to the Holocene (0.8 versus 1.1). This difference may be explained by an uneven  
709 geographical distribution of data points between the two datasets and a non-  
710 comparable timeframe (a 5000-year interval versus snapshots from the past two  
711 decades).

712

713 In summary, these statistical tests show that the modern seawater, late Holocene,  
714 and LGM datasets all form normal distributions. The late Holocene and LGM  
715 datasets have similar variances and so are indistinguishable in both width and type  
716 of distribution but differ in absolute composition. The deglacial dataset differs from all  
717 other datasets.

718

719 **Constraints on past NAC  $\epsilon\text{Nd}$ .** The past NAC composition likely remained  
720 unradiogenic, as today surface to sub-surface  $\epsilon\text{Nd}$  in the sub-polar N. Atlantic gyre  
721 are influenced by conservative mixing with very unradiogenic glacial and riverine  
722 inputs from N. America and Greenland, which is set by the unradiogenic bedrock  
723 composition of these regions<sup>73</sup>. Although surface water  $\epsilon\text{Nd}$  tends to be much more  
724 variable, and affected by wind-blown inputs, strong advection in subsurface Atlantic  
725 waters in the modern sub-polar gyre also appear to lead to much more conservative  
726  $\epsilon\text{Nd}$  behavior<sup>73</sup>.

727

728 **Data availability:** All data from this study can be found in the supplementary  
729 information (data tables) and can be accessed through the PANGAEA data archive.

730

731 **Code availability:** All modelling and statistical analysis was carried out with the use  
732 of published open-access software in R, as referenced in the methods. R codes  
733 used for the numerical procedures are available from the corresponding author upon  
734 reasonable request.

735

### 736 **Methods-only references**

737

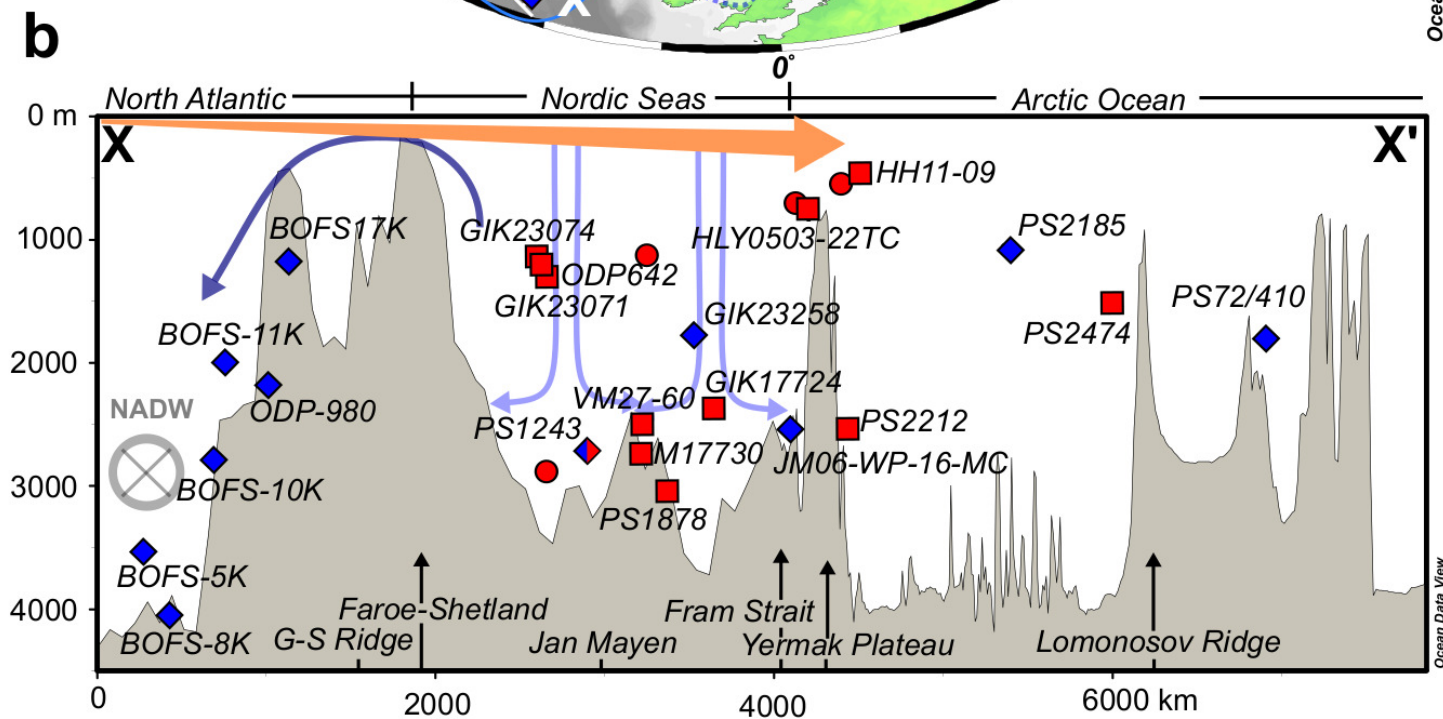
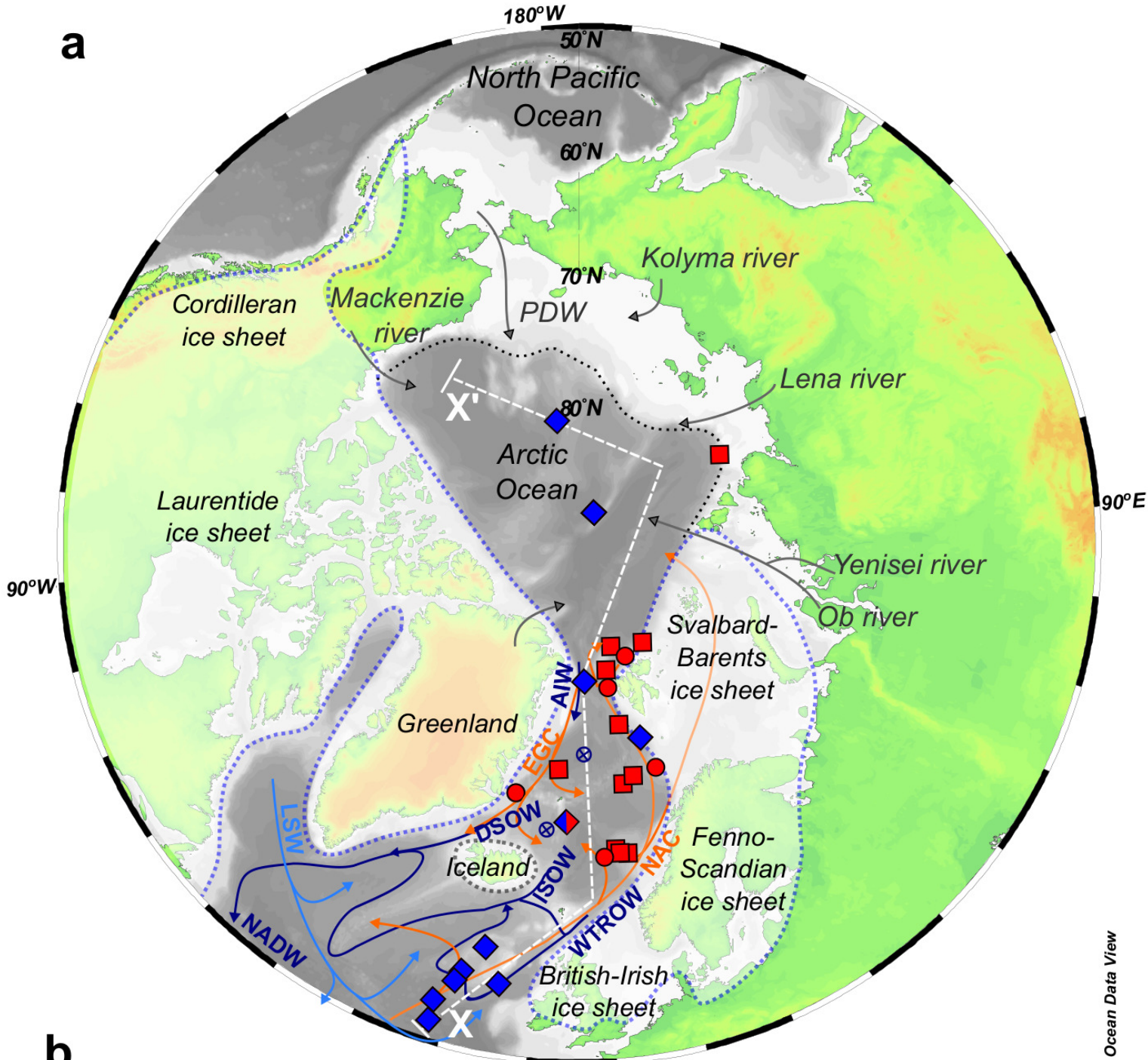
- 738 51. Blaser, P. *et al.* Extracting foraminiferal seawater Nd isotope signatures from  
739 bulk deep sea sediment by chemical leaching. *Chem. Geol.* **439**, 189–204 (2016).
- 740 52. Wilson, D. J., Piotrowski, A. M., Galy, A. & Clegg, J. A. Reactivity of  
741 neodymium carriers in deep sea sediments: Implications for boundary exchange  
742 and paleoceanography. *Geochim. Cosmochim. Acta* **109**, 197–221 (2013).
- 743 53. Tanaka, T. *et al.* JNdi-1: a neodymium isotopic reference in consistency with  
744 LaJolla neodymium. *Chem. Geol.* **168**, 279–281 (2000).
- 745 54. Jacobsen, S. B. & Wasserburg, G. J. Sm-Nd isotopic evolution of chondrites.  
746 *Earth Planet. Sci. Lett.* **50**, 139–155 (1980).
- 747 55. Weis, D. *et al.* High-precision isotopic characterization of USGS reference  
748 materials by TIMS and MC-ICP-MS. *Geochem. Geophys. Geosystems* **7**, Q08006  
749 (2006).
- 750 56. Hindshaw, R. S., Aciego, S. M., Piotrowski, A. M. & Tipper, E. T. Decoupling  
751 of dissolved and bedrock neodymium isotopes during sedimentary cycling.  
752 *Geochem. Perspect. Lett.* 43–46 (2018) doi:10.7185/geochemlet.1828.
- 753 57. Blaser, P. *et al.* The resilience and sensitivity of Northeast Atlantic deep water  
754  $\epsilon$ Nd to overprinting by detrital fluxes over the past 30,000 years. *Geochim.*  
755 *Cosmochim. Acta* **245**, 79–97 (2019).

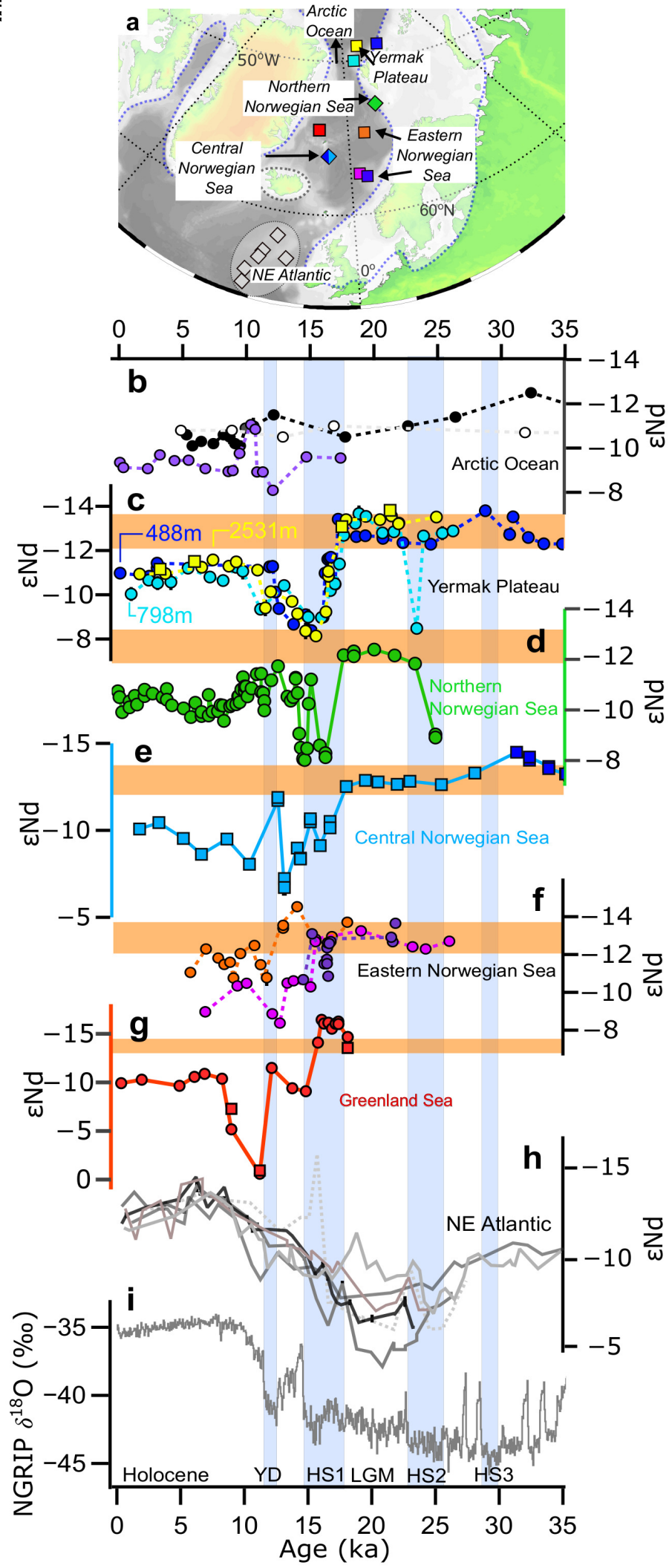
- 756 58. Sarnthein, M., Balmer, S., Grootes, P. & Mudelsee, M. Planktic and Benthic  
757 14C Reservoir Ages for Three Ocean Basins, Calibrated by a Suite of 14C  
758 Plateaus in the Glacial-to-Deglacial Suigetsu Atmospheric 14C Record.  
759 *Radiocarbon* **57**, 129–151 (2015).
- 760 59. Bronk Ramsey, C. *et al.* A Complete Terrestrial Radiocarbon Record for 11.2  
761 to 52.8 kyr B.P. *Science* **338**, 370–374 (2012).
- 762 60. Heaton, T. J. *et al.* Marine20—The Marine Radiocarbon Age Calibration  
763 Curve (0–55,000 cal BP). *Radiocarbon* **62**, 779–820 (2020).
- 764 61. Blaauw, M. & Christen, J. A. Flexible paleoclimate age-depth models using an  
765 autoregressive gamma process. *Bayesian Anal.* **6**, 457–474 (2011).
- 766 62. *Proceedings of the Ocean Drilling Program, 104 Scientific Results*. vol. 104  
767 (Ocean Drilling Program, 1989).
- 768 63. Stein, R. *et al.* Accumulation of particulate organic carbon at the Eurasian  
769 continental margin during late Quaternary times: controlling mechanisms and  
770 paleoenvironmental significance. *Glob. Planet. Change* **31**, 87–104 (2001).
- 771 64. Vogelsang, E., Sarnthein, M. & Pflaumann, U.  $\delta^{18}\text{O}$  Stratigraphy, chronology,  
772 and sea surface temperatures of Atlantic sediment records (GLAMAP-2000 Kiel).  
773 *Berichte - Rep. Inst. Für Geowiss. Christ.-Albrechts-Univ. Kiel* (2001).
- 774 65. Mangerud, J. & Gulliksen, S. Apparent Radiocarbon Ages of recent marine  
775 shells from Norway, Spitsbergen, and Arctic Canada. *Quat. Res.* **5**, 263–273  
776 (1975).
- 777 66. Xuan, C., Channell, J. E. T., Polyak, L. & Darby, D. A. Paleomagnetism of  
778 Quaternary sediments from Lomonosov Ridge and Yermak Plateau: implications  
779 for age models in the Arctic Ocean. *Quat. Sci. Rev.* **32**, 48–63 (2012).

- 780 67. Vogt, C., Knies, J., Spielhagen, R. F. & Stein, R. Detailed mineralogical  
781 evidence for two nearly identical glacial/deglacial cycles and Atlantic water  
782 advection to the Arctic Ocean during the last 90,000 years. *Glob. Planet. Change*  
783 **31**, 23–44 (2001).
- 784 68. Svensson, A. *et al.* A 60 000 year Greenland stratigraphic ice core  
785 chronology. *Clim. Past* **4**, 47–57 (2008).
- 786 69. Dokken, T. M. & Jansen, E. Rapid changes in the mechanism of ocean  
787 convection during the last glacial period. *Nature* **401**, 458–461 (1999).
- 788 70. Telesiński, M. M., Bauch, H. A., Spielhagen, R. F. & Kandiano, E. S. Evolution  
789 of the central Nordic Seas over the last 20 thousand years. *Quat. Sci. Rev.* **121**,  
790 98–109 (2015).
- 791 71. Voelker, A. H. L. *et al.* Correlation of Marine 14C Ages from the Nordic Seas  
792 with the GISP2 Isotope Record: Implications for 14C Calibration Beyond 25 ka BP.  
793 *Radiocarbon* **40**, 517–534 (1997).
- 794 72. Weinelt, M. *et al.* Variability of North Atlantic heat transfer during MIS 2.  
795 *Paleoceanography* **18**, (2003).
- 796 73. Lambelet, M. *et al.* Neodymium isotopic composition and concentration in the  
797 western North Atlantic Ocean: Results from the GEOTRACES GA02 section.  
798 *Geochim. Cosmochim. Acta* **177**, 1–29 (2016).

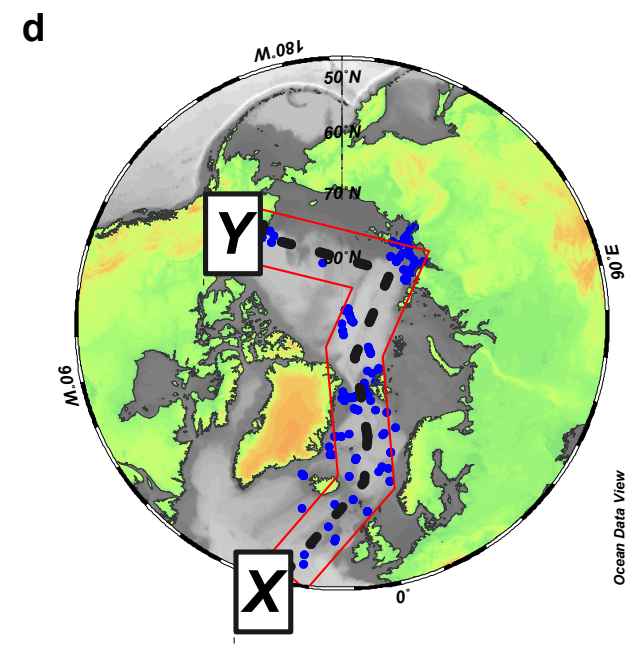
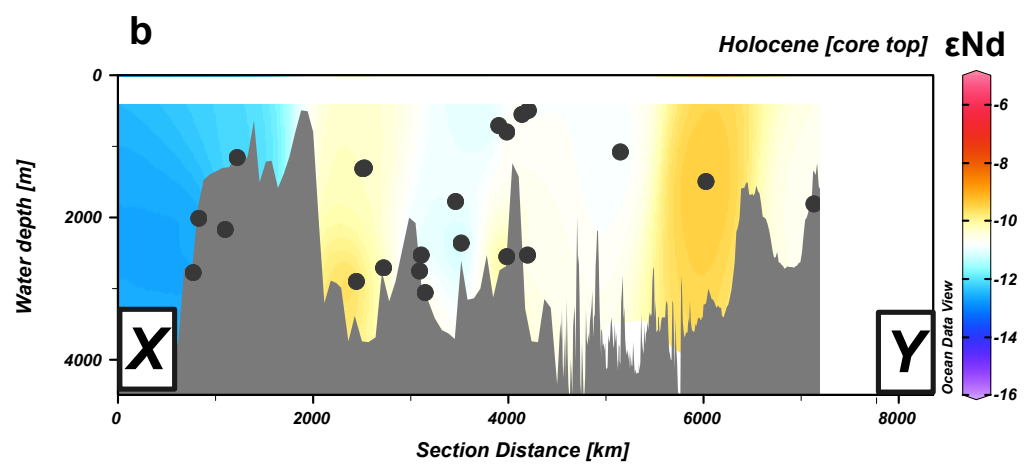
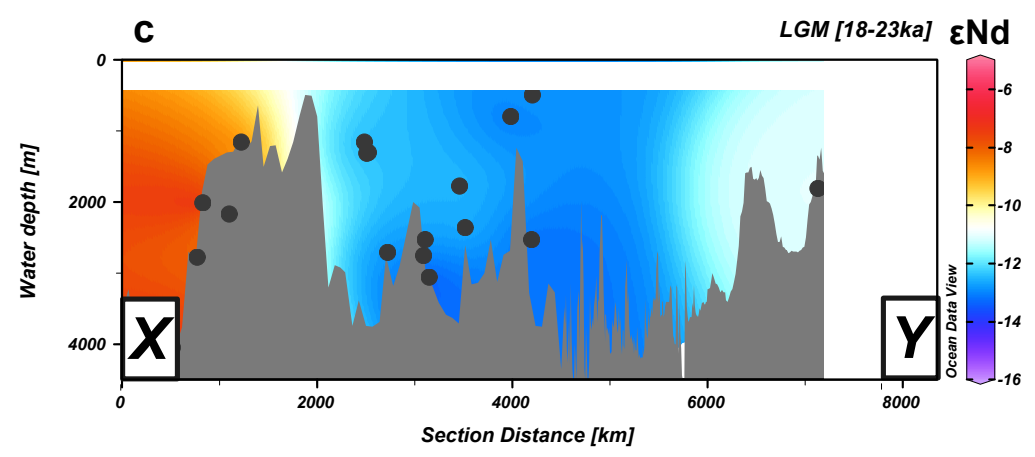
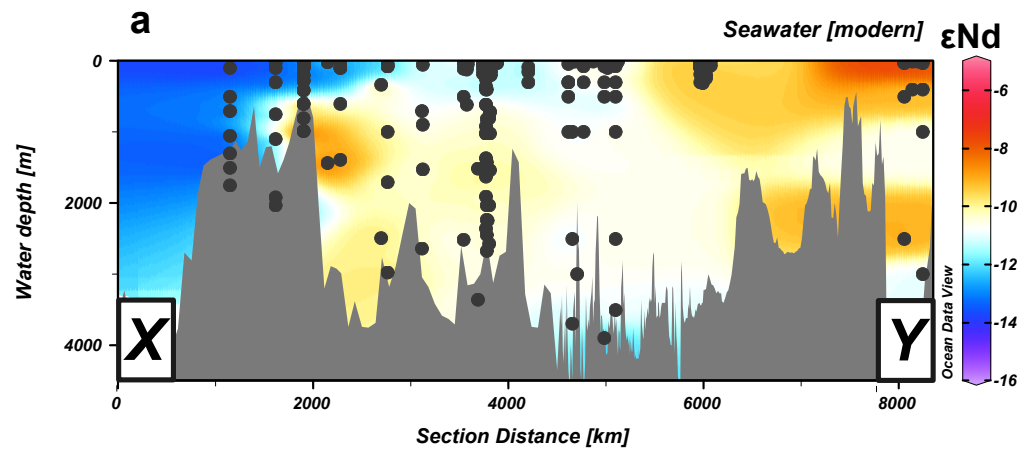
799

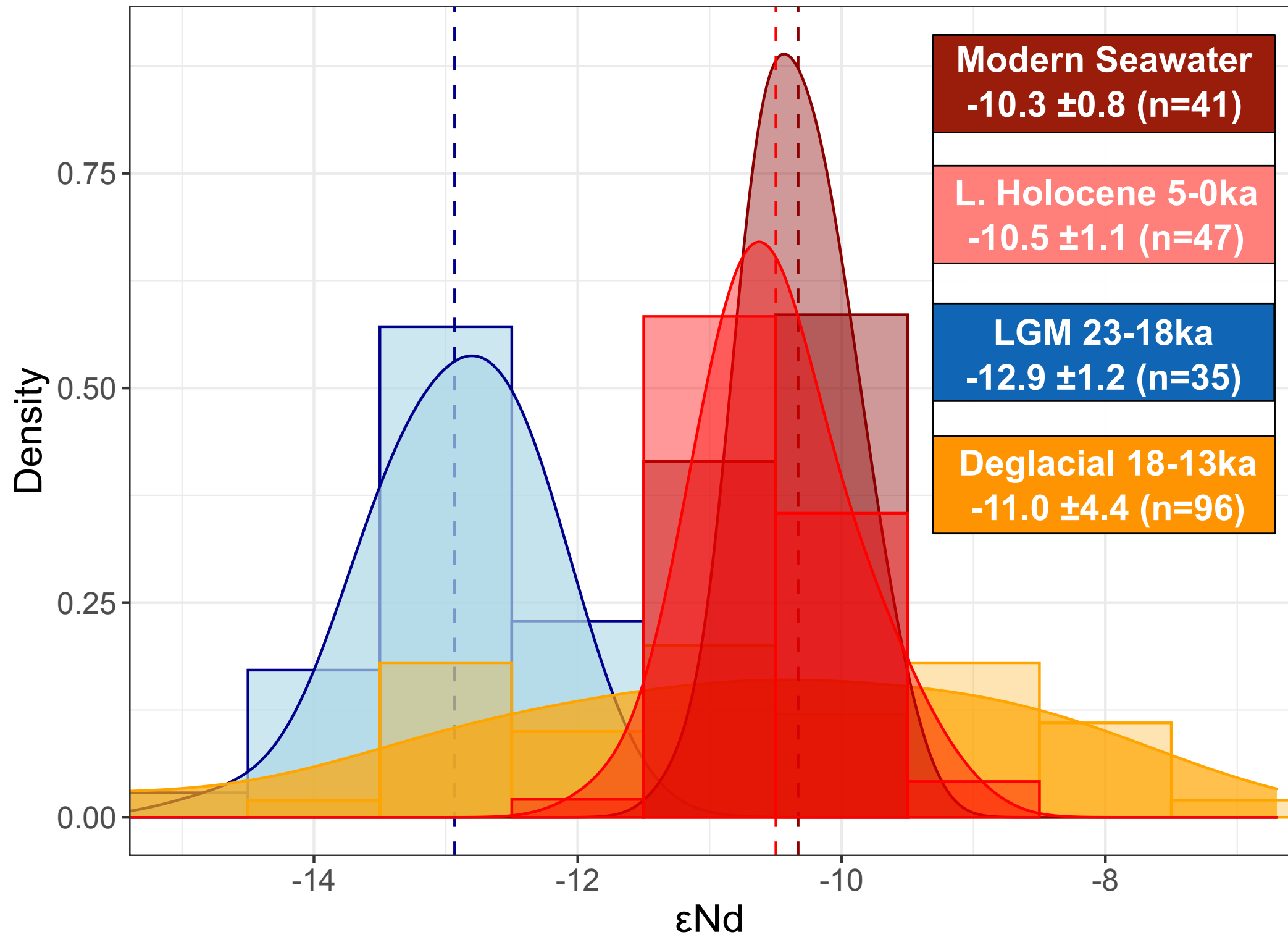
800



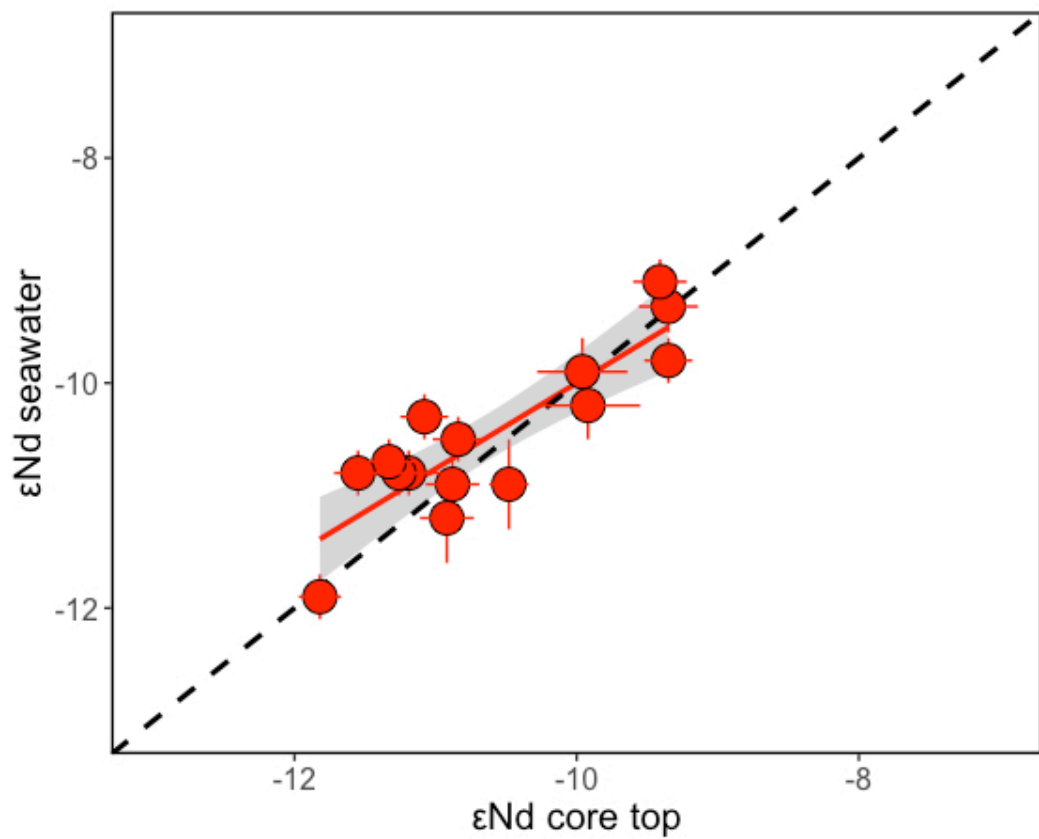
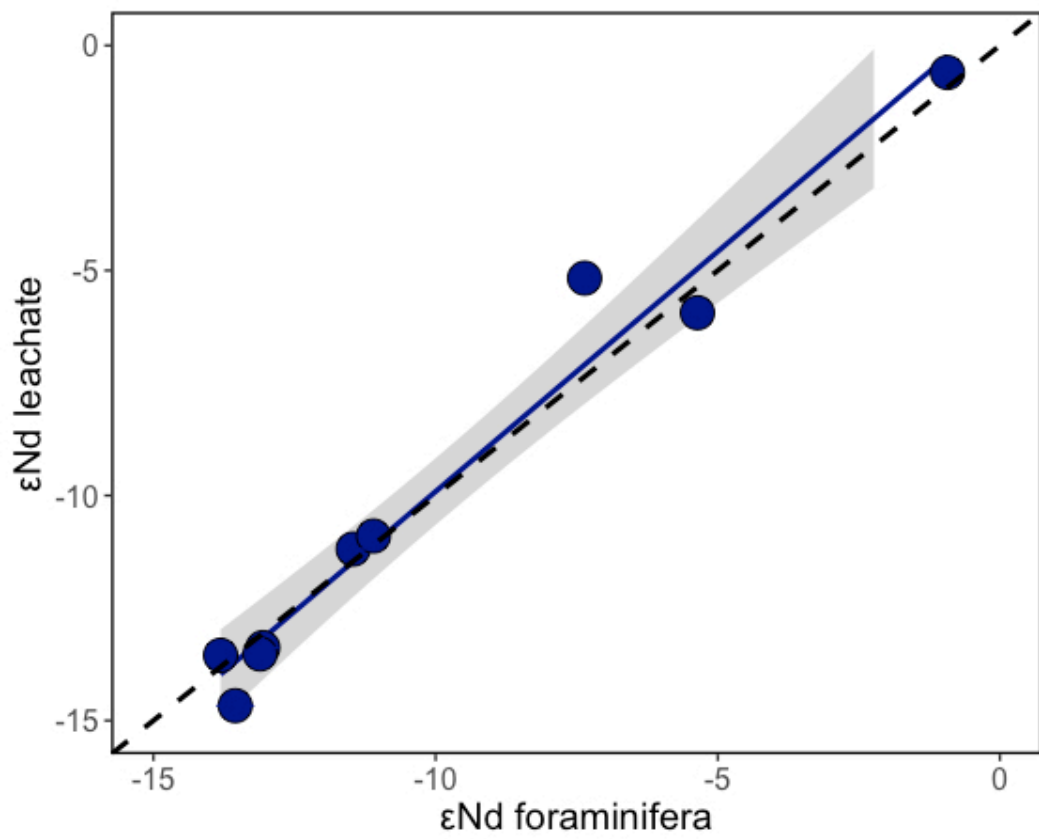


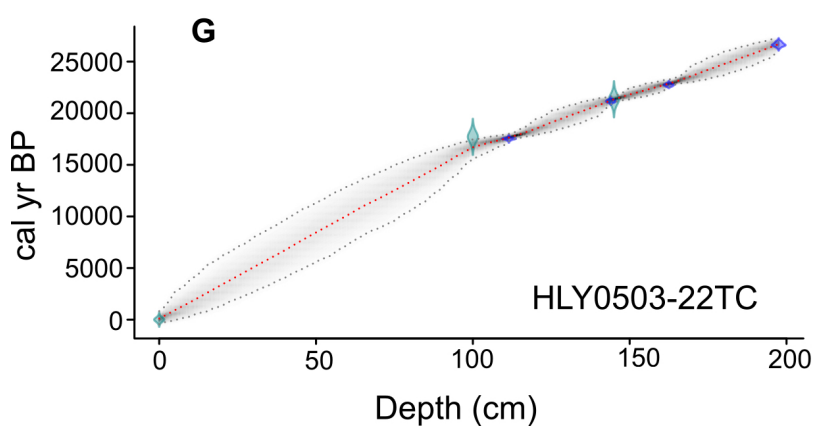
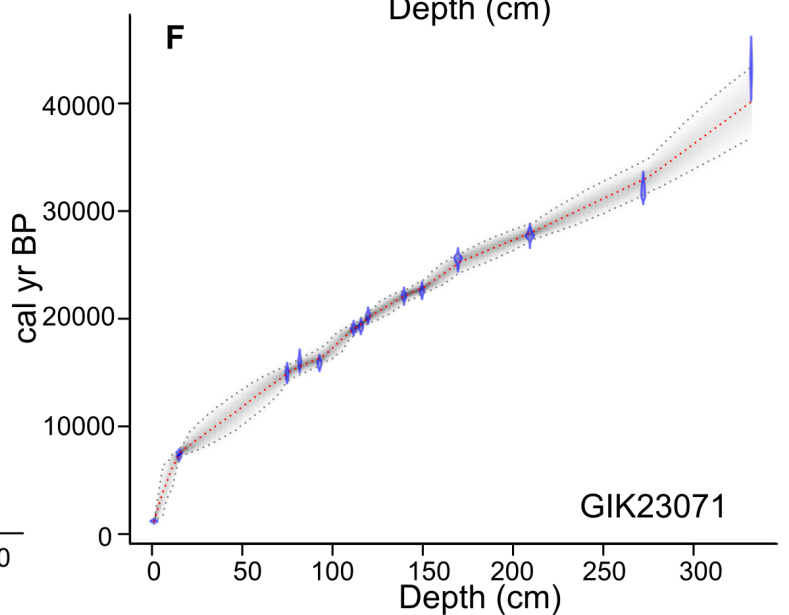
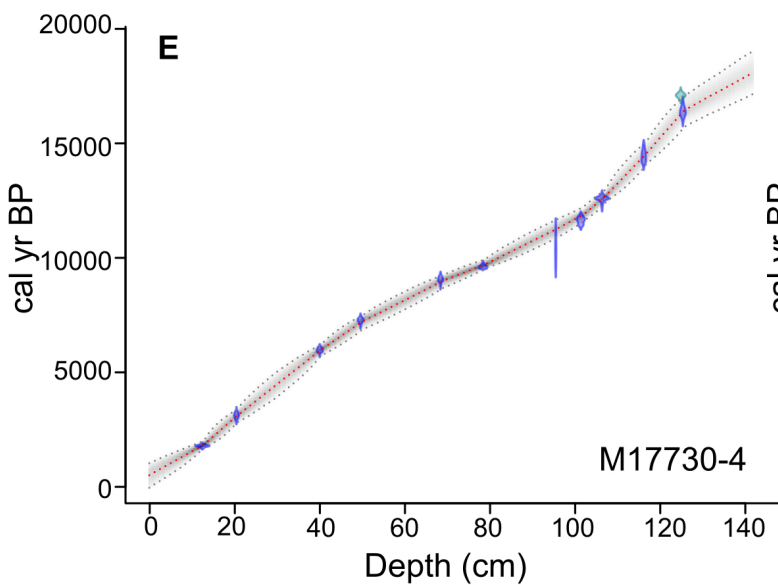
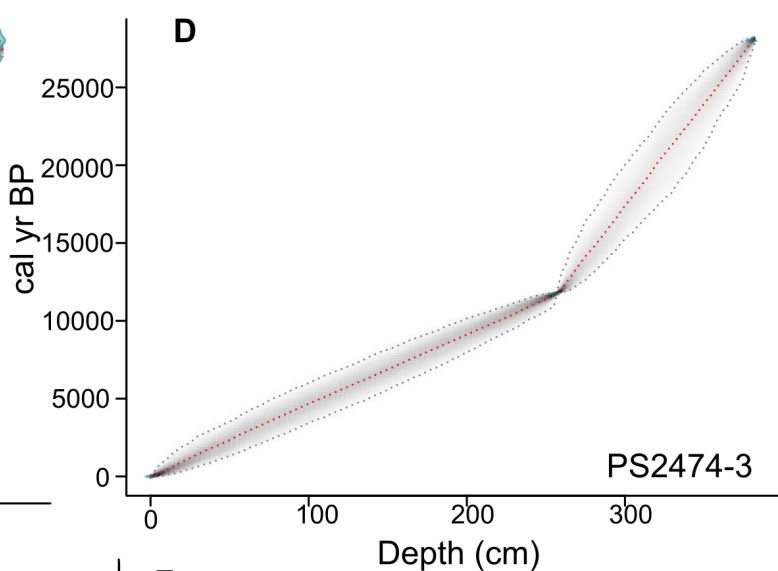
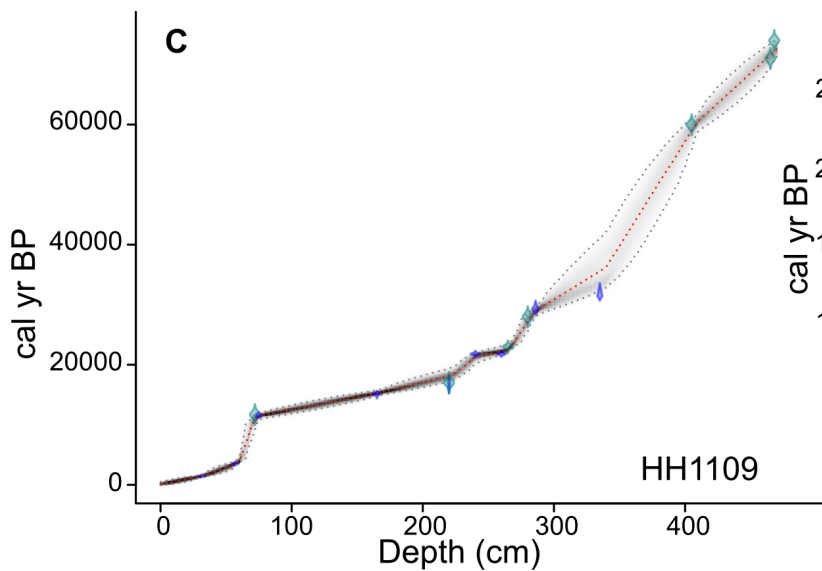
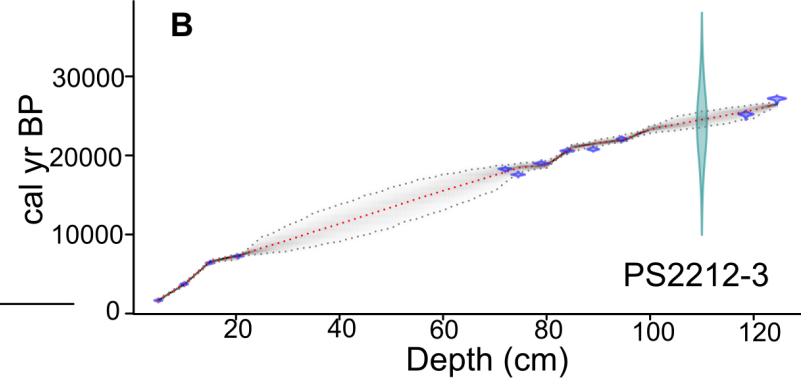
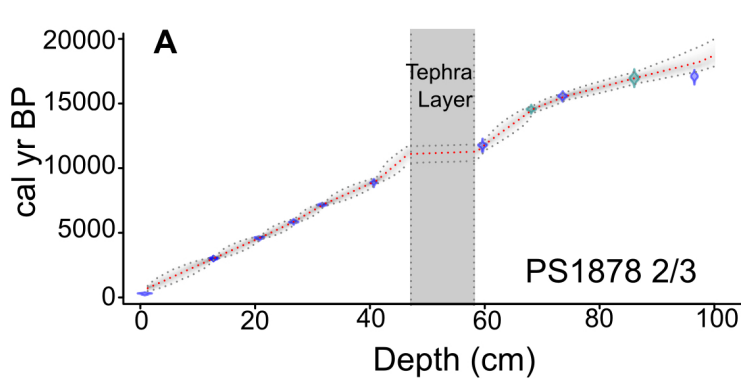


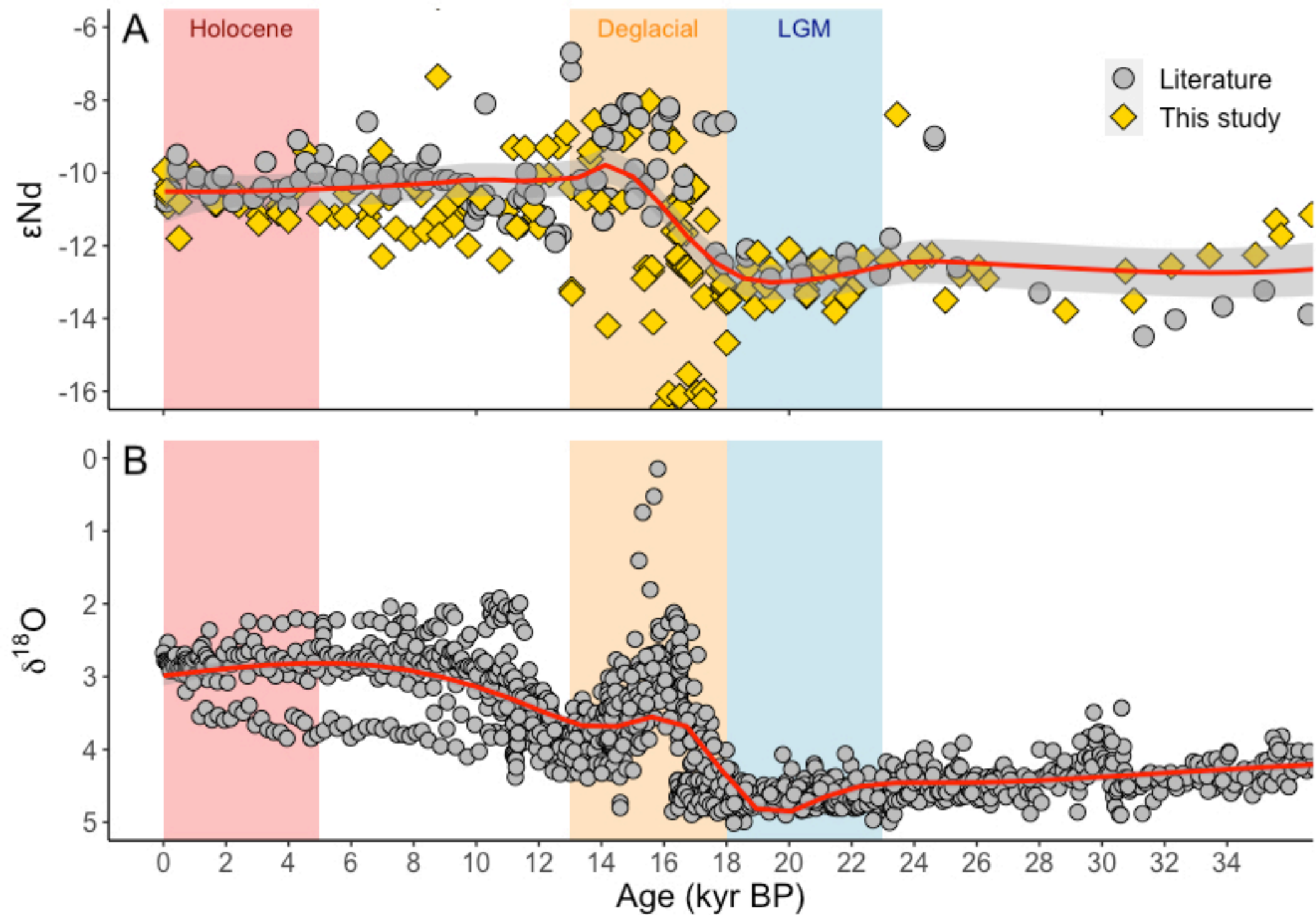


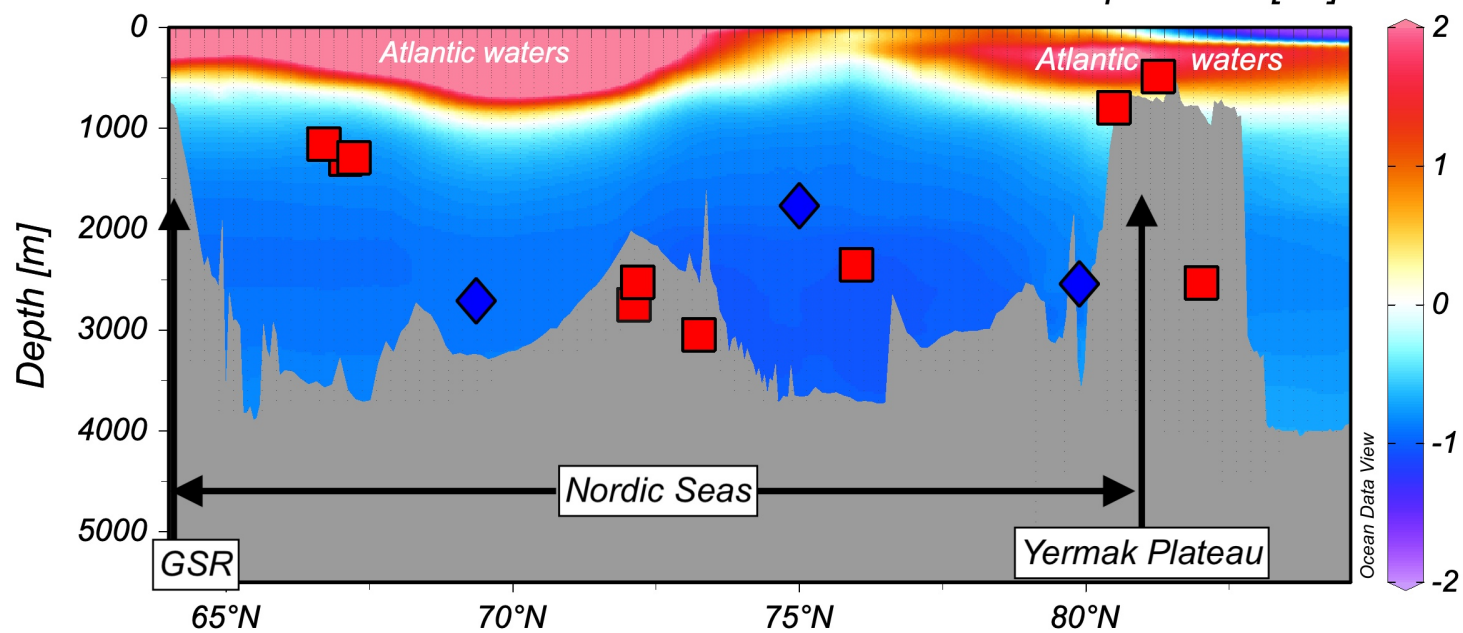
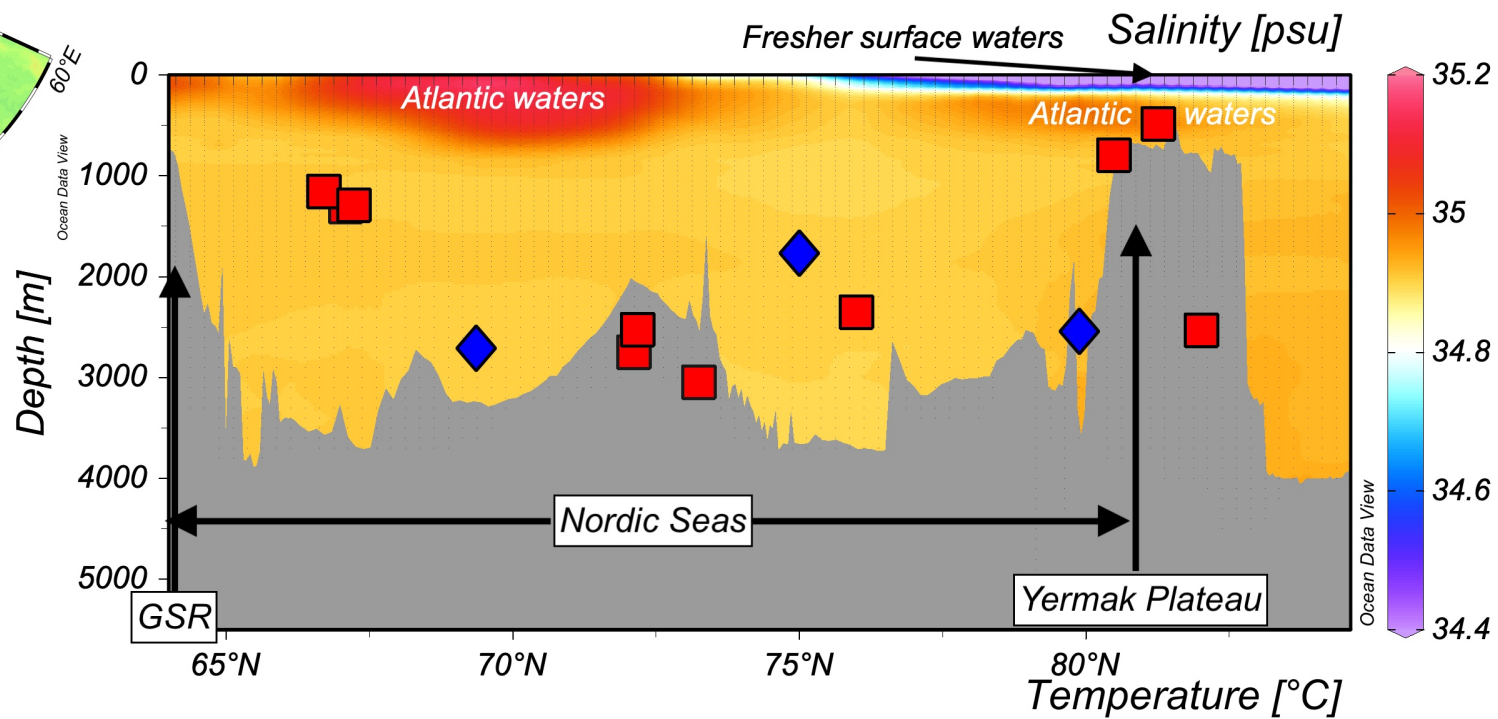
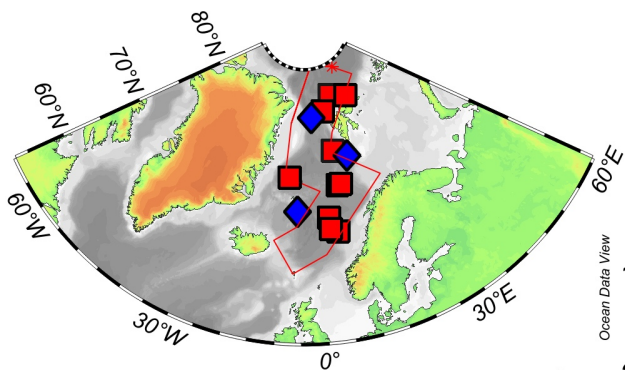


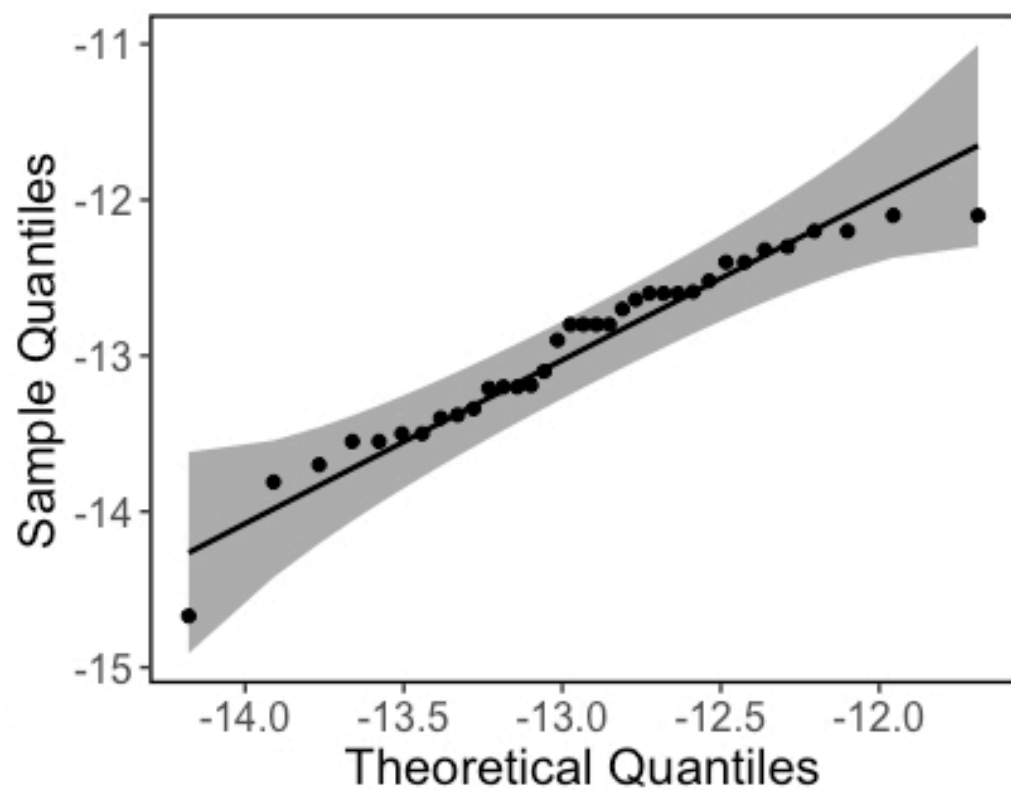
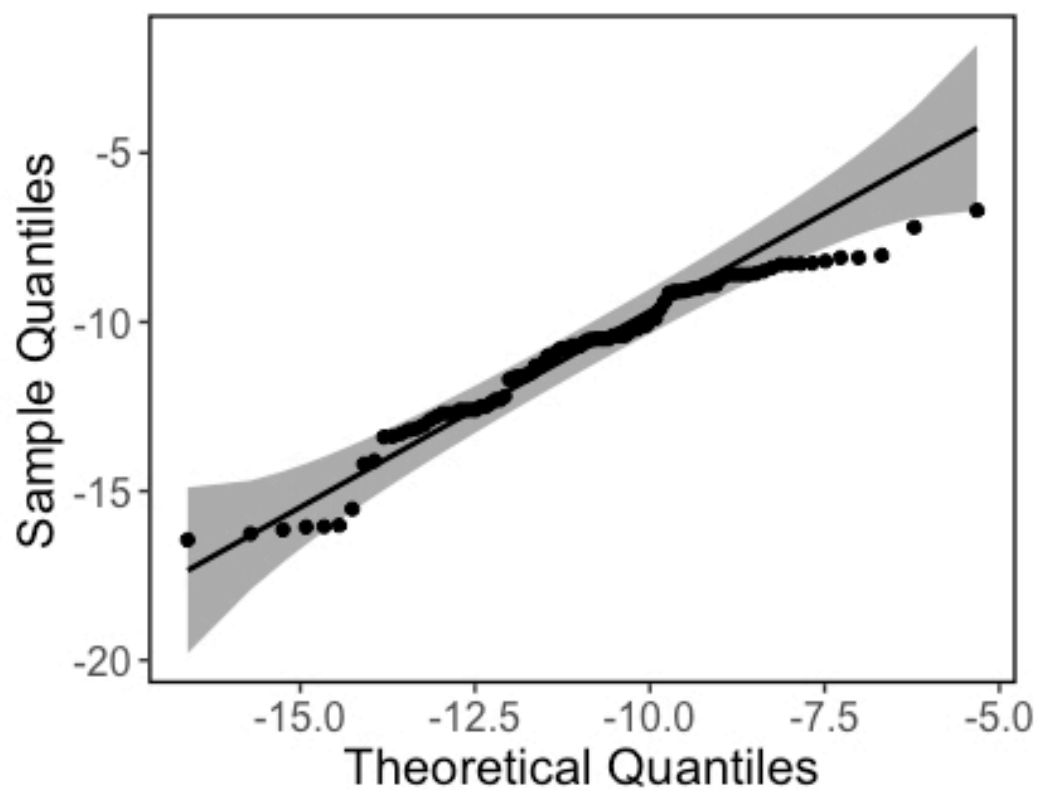
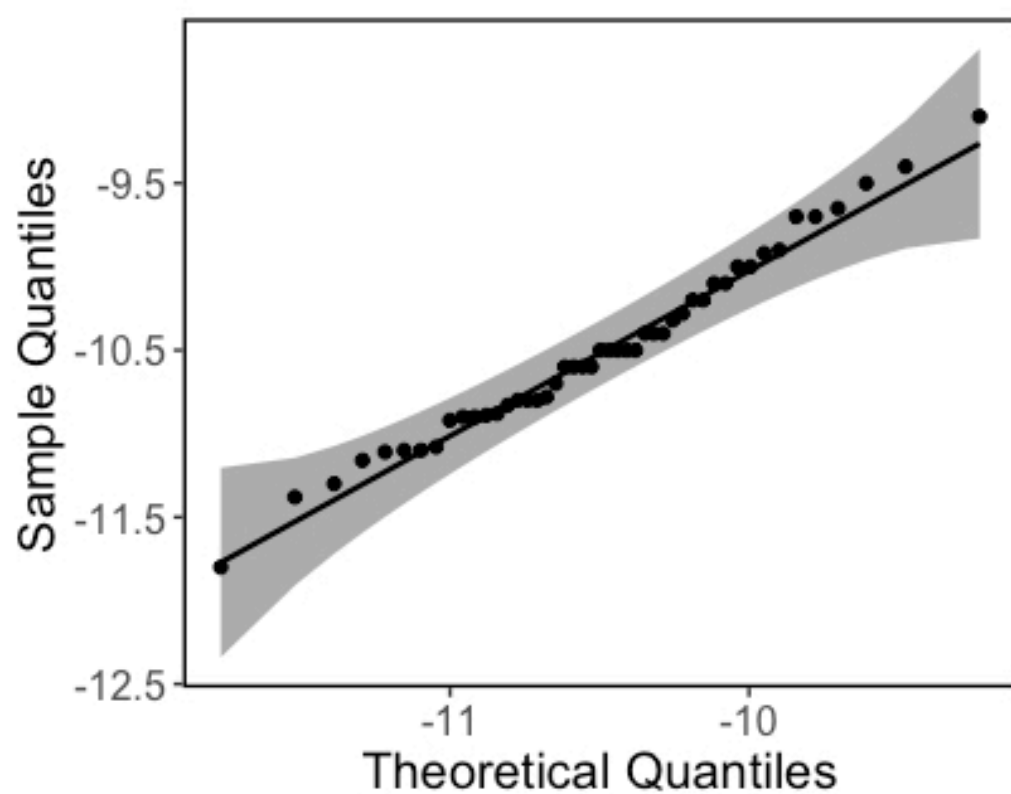
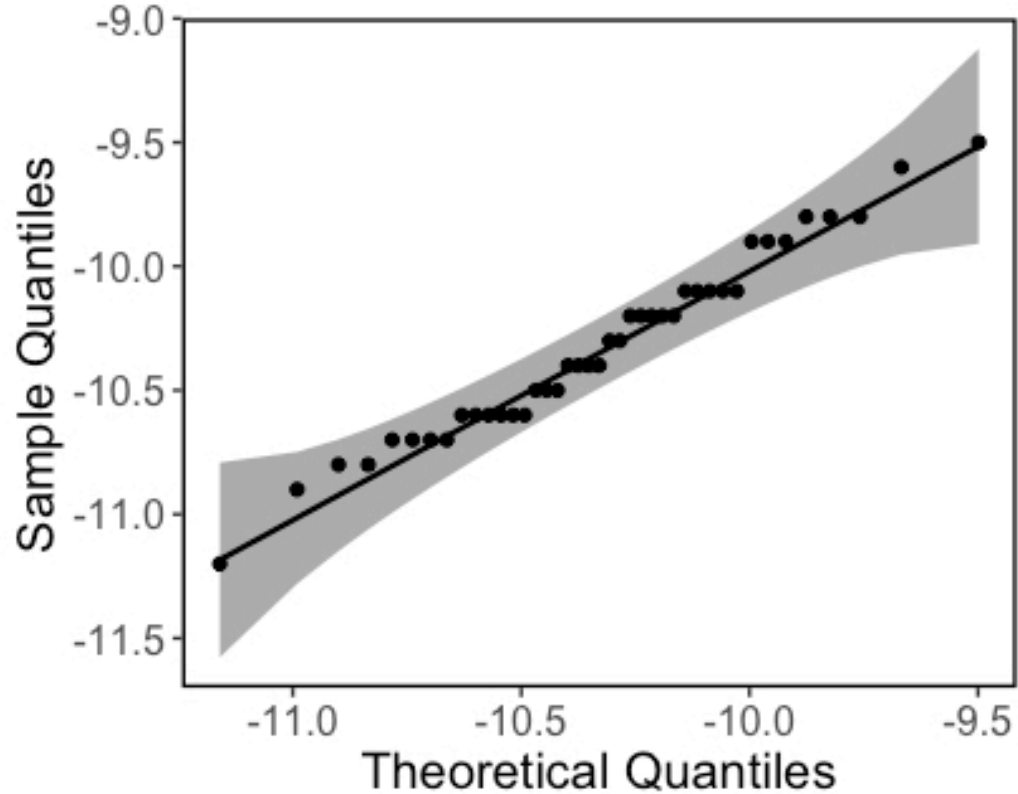












---

<b><math>\epsilon</math>Nd Sample set</b>	<b>Shapiro-Wilk test statistic, W</b>	<b><i>p</i>-value</b>
Modern Seawater	0.97951	0.6569
Late Holocene	0.98420	0.7579
Deglacial	0.95141	0.0010
LGM	0.94955	0.1291

---

---

**$\epsilon$ Nd sample sets  
compared**

**F-test statistic**

***p*-value**

---

Late Holocene and  
modern seawater

0.44982

0.0113

LGM and late Holocene

1.072218

0.8157

---